

Enumeration of all superconducting circuits up to 5 nodes

Eli J. Weissler,^{1,*} Mohit Bhat,¹ Zhenxing Liu,² and Joshua Combes^{1,3}

¹Electrical, Computer, and Energy Engineering, University of Colorado Boulder, Colorado 80309, USA

²Materials Science and Engineering, University of Colorado Boulder, Colorado 80309, USA

³School of Physics and School of Mathematics, The University of Melbourne, VIC 3010, Australia

(Dated: October 25, 2024)

Nonlinear superconducting circuits can be used as amplifiers, transducers, and qubits. Only a handful of superconducting circuits have been analyzed or built, so many high-performing configurations likely remain undiscovered. We seek to catalog this design space by enumerating all superconducting circuits – up to five nodes in size – built of capacitors, inductors, and Josephson junctions. Using graph isomorphism, we remove redundant configurations to construct a set of unique circuits. We define the concept of a “Hamiltonian class” and sort the resulting circuit Hamiltonians based on the types of variables present and the structure of their coupling. Finally, we search for novel superconducting qubits by explicitly considering all three node circuits, showing how the results of our enumeration can be used as a starting point for circuit design tasks.

I. INTRODUCTION

Classical nonlinear circuits have been explored and categorized for over a century [1, 2]. Large, complex analog and digital circuits are often constructed by connecting smaller well-understood circuits [3]. These smaller circuits or modules, usually with fewer than 10 nonlinear elements, are made for specific functions. Within the process of discovering and designing these modules, three key concepts are closely intertwined (also outlined in Fig. 1):

1. **CIRCUIT ENUMERATION** uses a combinatorial approach to list all unique circuit configurations, given a set of components.
2. **CIRCUIT SYNTHESIS** constructs a circuit that meets performance requirements, subject to constraints.
3. **CIRCUIT EQUIVALENCE** determines if circuits perform the same function, despite different configurations.

These ideas are intertwined because it is difficult to synthesize performant new circuits if a procedure suggests circuits equivalent to previously examined ones, or if it cannot explore new circuit topologies.

Superconducting quantum circuits have gained widespread use over the last 25 years as qubits, amplifiers, and transducers [4]. Most devices have been built from a small library of simple circuits, perhaps due to a lack of known applications or challenges in control and fabrication for larger circuits. For example, the most widely used superconducting qubit today, the transmon, is at its core a Josephson junction in parallel with a capacitor. Large-scale industrial efforts in superconducting quantum computing use this basic design, building complex systems by repeating the transmon several times. With the design, fabrication,

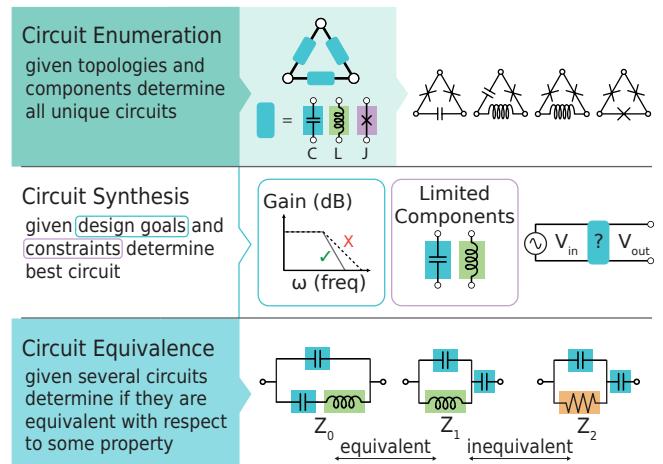


FIG. 1. Visual representations of circuit enumeration, synthesis, and equivalence. The aim of our work is to enumerate all unique nonlinear quantum circuits with up to 5 nodes. The results of our enumeration leverage circuit equivalence and can be used in circuit synthesis tasks to find new qubits and amplifiers. In the circuit synthesis example, we desire a low pass filter with a certain roll-off and search for a LC circuit that has this property. The circuit equivalence depicted is with respect to impedance Z_i .

and control knowledge gained over the last two decades, we are now in the position to explore larger quantum circuits.

This paper seeks to catalogue this under-explored space by explicitly enumerating all superconducting circuits consisting of capacitors, inductors, and Josephson junctions.¹ We consider up to five nodes due to computational constraints, although the procedure could be applied to larger circuits. Using the results of our enu-

¹ It is easy to include other two terminal devices such as the Quantum Phase Slip junction, but difficult to include three or more terminal devices see appendix A 4 for more details.

* eli.weissler@colorado.edu

meration, it is possible to more efficiently approach circuit design or synthesis tasks. As an example, we will search for novel superconducting qubits by considering all possible three node circuits.

The remainder of this paper is structured as follows. In Sec. II we give brief historical context for circuit enumeration and summarize related work. In Sec. III, we describe our enumeration algorithm, which leans on the work by Herber *et al.* [5, 6] to create a set of unique circuits. In Sec. IV we introduce the concept of Hamiltonian enumeration and reduction, as a way to classify the resulting Hamiltonians into qualitatively similar “classes.” Then in Sec. V, we present our circuit and Hamiltonian enumeration results. Then we begin to apply our results to the search for new qubits. We start by developing a numerical procedure, in Sec. VI, to estimate a circuit’s performance as a qubit and then optimize the performance with respect to the underlying circuit parameters. In Sec. VII, we then use this method to search through our enumerated set of three node circuits for new qubits. This work relies on existing circuit quantization software packages [7–13]. In Sec. VIII we conclude with some open problems.

II. HISTORICAL PERSPECTIVE & RELATED WORK

In the late 1800s, circuit enumeration became important due to the explosion of the telephone network. According to Darlington’s account [14]: Foster and Campbell [15], while exploring four-port transformer circuits, initially aimed to patent some promising designs. However, their patent department advised against patenting designs where equivalent circuits existed. Upon realizing the vast number of possible circuits (83,539), they opted to publish the enumeration, ensuring these designs remained unpatented and open for use.

The field of circuit enumeration has been and continues to be very active [5, 6, 16–28]. Most work has focused on circuits for specific applications with two-terminal, passive linear elements, although there has been some success considering nonlinear and multiport devices [29–31]. One set of efforts have discovered useful previously-unknown amplifier circuits [32–35]. Recent work has aimed to integrate machine learning and advanced optimization methods into more traditional enumeration and synthesis [36–38].

The systematic study of quantum circuit theory (circuit Quantum Electrodynamics [4] or circuit QED) was kicked off by Yurke and Denker [39]. The body of this work is largely disconnected from classical circuit theory, because analyzing quantum circuits requires the use of Lagrangian and Hamiltonian mechanics, a formalism rarely used by electrical engineers [40–42]. The field of circuit QED has blossomed, largely due to experimental breakthroughs in the early 2000s [43–48] and over the past two decades [49–51].

The field has mainly focused on superconducting qubits, due to their importance in quantum computing. The most famous circuit is a capacitor in parallel with a Josephson junction [43, 52]. By optimizing the values of the capacitance and Josephson energy, the coherence time has gone from nanoseconds [43] to the median T_1 and T_2^{echo} , both at ~ 0.5 milliseconds [53]. Improvements in materials and fabrication have contributed to this increase as well.

The majority of superconducting circuits built today are similarly small two-node circuits made of capacitors (C), inductors (L), and Josephson junctions (J). In particular the resonator – LC, the transmon – CJ, and fluxonium – CJL [54, 55]. However, more work has begun to focus on larger, more complicated circuits. This interest largely stems from the subfield of “protected qubits” [56], where it has been shown that a larger (3+ node) circuit is necessary to achieve robust protection against both energy relaxation and pure dephasing [57]. Identifying the best qubits within this set of 3+ node circuits remains an open question. Our work represents a method to catalog all these possibilities.

Finally, we would like to place our effort in the context of related work in superconducting quantum circuit design. Most work has been largely concerned with either optimizing a particular design or with synthesizing a single performant circuit. For example, Yan *et al.* [58] consider a generalized flux qubit and use approximations to analytically explore the design space. While their analysis captures many previous qubit designs, it does not apply to more complicated circuit topologies. In Ref. [59], Lui *et al.* use a variational quantum algorithm to optimize the component values of a parallel CJL circuit, where the cost function is a weighted sum of the qubit frequency and anharmonicity.

Mirroring trends in classical circuit theory, many recent works have focused on integrating machine learning and other advanced optimization methods into the design process. The work of Menke *et al.* [60] uses a closed loop swarm optimization algorithm to optimize desired circuit properties, given a circuit topology to work from. Cárdenas-López *et al.* [61] uses genetic algorithms to design noise resilient qubits with particular selection rules. In related work by some of the same authors, this algorithm is used to design a new four-node qubit called the “Difluxmon” [62]. Rajabzadeh *et al.* [63] develops gradient based optimization of superconducting circuits. They then optimize circuit design with respect to an upper bound on the number of gates within a single coherence time (similar to the metric we consider in Sec. VI), considering unique circuit topologies separately. Finally, Kumar *et al.* [64] uses graph machine learning methods to approach the circuit synthesis problem.

Apart from Ref. [63], previous work is mainly focused on optimizing a single design for a particular use. In contrast, our work aims to capture a broader perspective by cataloging the entire design space in the style of Foster and Campbell. The results of our enumeration study can

then be used as an advanced starting point for any circuit synthesis task.

III. CIRCUIT ENUMERATION ALGORITHM

Our enumeration procedure is split into two steps:

1. *Combinatorial enumeration.*

First, we represent circuit topologies using a unique set of undirected graphs. Each edge can support a two-terminal circuit component, like a capacitor. For each circuit topology, we consider all possible combinations of components on the edges.

2. *Reduction of equivalent configurations.*

The set of circuits generated in step 1 will contain many equivalent circuits (e.g. two capacitors in series). We identify these configurations and reduce them to a smaller set of “unique” circuits.

The remainder of this section provides details on these two steps. A graphical summary of this enumeration procedure is depicted in Fig. 2. We note that our procedure builds on the work by Herber et al. [5, 6].

A. Combinatorial Enumeration

Our combinatorial enumeration procedure will produce all possible circuit configurations up to n nodes, given a list of two-terminal reciprocal devices. Here we consider linear capacitors (C), linear inductors (L), and Josephson junctions (J) which are nonlinear inductors. These circuit elements are the most widely fabricated in superconducting circuits.

These circuits can be thought of as undirected graphs, where the edges support two-terminal components, and the vertices are circuit nodes. We begin our enumeration with the set of unique circuit topologies, defined by the minimal set of non-isomorphic, connected, undirected graphs (we use those from Brendan McKay’s combinatorial database [65]). We refer to these graphs as “base graphs” because they form the starting point of our enumeration. In Fig. 3 we see that there are 1, 2, 6, and 21 possible topologies for circuits consisting of two, three, four, and five nodes. This number grows to 112 for six nodes, 853 for seven nodes, and 11,117 for eight nodes.

The next step is to substitute in circuit elements for each edge on each base graph. Consider a base graph with N_E edges and m two-terminal components. For the two vertex base graph, there are m possible circuits. In our enumeration, we allow for $m = 7$ total options, comprised of parallel combinations of our original three elements. The string representations of the elements are,

$$C, J, L, CJ, CL, JL, \text{ and } CJL. \quad (1)$$

In general, the enumeration is performed by counting in base- m . Such that each possible configuration is represented by a base- m string of length N_E . The total

number of configurations for a base graph with N_E edges is thus $m^{N_E} = 7^{N_E}$. There are two base graphs for three node circuits, one with two edges, and one with three edges. The total number of possible configurations for three node circuits is thus $7^3 + 7^2 = 392$. Similarly, summing up the contributions from all base graphs for four and five nodes, the number of configurations swells to 139,944, and 338,332,113 respectively.

Many generated circuit configurations will be equivalent; reducing them to a minimal set of “unique” circuits is discussed in Sec. III B.

B. Reduction of Equivalent Configurations

To identify a minimal set of “unique” circuits, we begin with the full set generated in section III and remove circuits that: are fully linear, contain series linear components, or are otherwise equivalent to another one in the set. In this subsection we will detail these three steps, which are also illustrated in Fig. 2.

1. *Fully Linear Circuits*

While linear circuits are important, they are well studied and require more complicated interactions for interesting applications. For example a qubit can be encoded in a linear circuit, like an LC resonator, but nonlinear interactions are needed for universal gates or to encode the qubit into a bosonic code [66–68]. Here, we focus on circuits that could be used directly as qubits, which require at least one nonlinear element. Therefore, we remove all circuits without Josephson junctions. In Fig. 2, reduction step 1, all fully linear are greyed out to show that they are removed in this step. The example shown is two capacitors and one inductor.

2. *Series Linear Components*

In classical circuit theory, two linear circuit elements of the same type in series are equivalent on the outer terminals to a single element with a new capacitance, inductance, or resistance. We remove all circuits where this type of series reduction is possible.

One might worry that this equivalence does not hold when considering the quantum treatment of the circuit. However, series capacitors or inductors correspond to capacitively or inductively shunted islands, or chunks of the circuit that are only connected to the rest of the circuit via linear capacitors or linear inductors. These islands correspond to non-dynamical “free” (capacitively shunted, has kinetic energy but no potential landscape) and “frozen” (inductively shunted, has a confining potential but no kinetic energy) variables in the circuit Lagrangian [8]. In the case of a single-node island, these

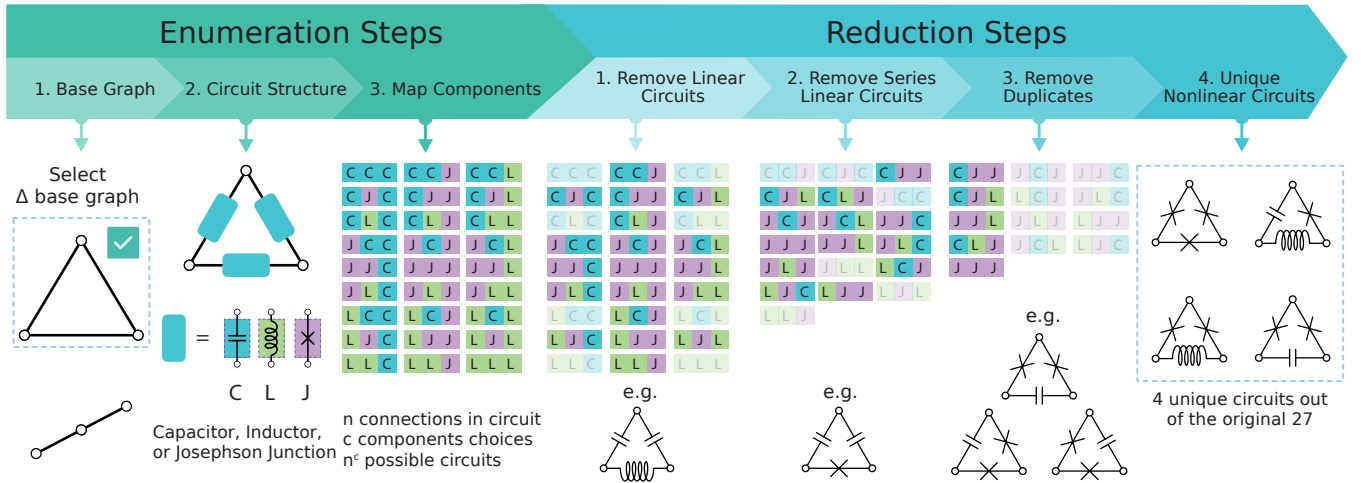


FIG. 2. Example circuit enumeration and reduction for three node circuits. **Enumeration:** (Step 1) For a given number of nodes, select a base graph. For $n = 3$ there are two options, and for this figure, we choose the Delta topology. (Step 2) Given the Delta topology, we allow each edge to one of m components. In this example, the edge can be either a capacitor, inductor, or Josephson junction. In general, we allow for combinations of our original three elements so the edges could be in the set $\{C, J, L, CL, JL, CJ, CJL\}$. (Step 3) We enumerate all possible m -ary strings, here there are 27 possible configurations. **Reduction:** Circuits that are eliminated at each step are grayed out. (Step 1) We remove any circuit that doesn't have a JJ because linear circuits are well understood. (Step 2) We remove circuits that have linear components in series because there is a circuit with one fewer node that is equivalent. (Step 3) Of the remaining circuits, several are identical, so we perform a graph isomorphism check to remove equivalent circuits. (Step 4) Four unique nonlinear circuits remain out of the original 27.

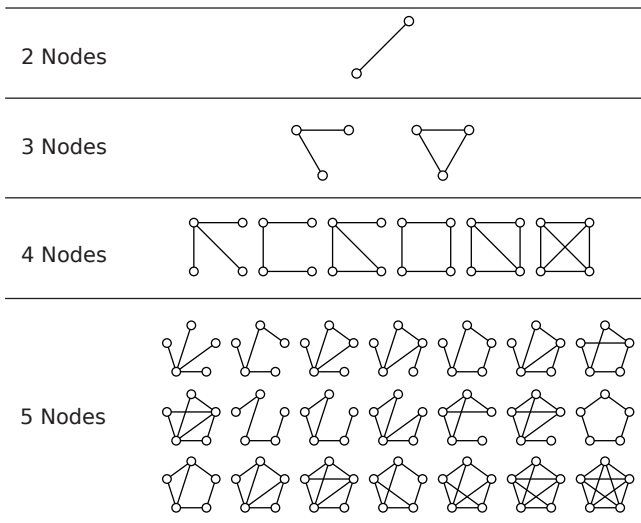


FIG. 3. Base graphs for circuits up to five nodes in size. Base graphs are the set of non-isomorphic, connected, undirected graphs with the specified number of vertices. Each base graph represents a unique circuit topology in our enumeration. Note that every base graph except for the fully connected five node can be drawn as a planar graph.

non-dynamical variables can be eliminated from the Lagrangian and reproduce the classical expressions for combining capacitors/inductors in series [69]. Another concern is that these islands are a natural place to couple e.g. a voltage drive. However, if the connection is linear,

one can equivalently couple to the outer nodes using the Δ -Y transform.

A simple example of combining linear elements is depicted in Fig. 2 in reduction step (2) where a junction in parallel with two capacitors is eliminated because it is equivalent to the transmon circuit.

3. Component-like Isomorphism

When two circuits are the same up to relabeling of nodes, they can be considered equivalent. In our reduction, only one circuit from each equivalent set is kept. In Fig. 2 reduction step 3, there are three total circuits with two JJ's and one capacitor: CJJ , JCJ , JJC . Due to the rotational symmetry of the base graph involved, the three are the same circuit, with their diagrams merely rotated relative to one another. As a result, only one (CJJ) is kept.

To systematically identify these equivalent circuits, we perform colored graph isomorphism on the “component graph” representation of the circuit. The component graph is a colored graph where each component and node in the circuit are represented by a vertex in the graph. All interchangeable parts are assigned the same color. In other words, all capacitors are the same color, all inductors are a different color, and all Josephson junctions are a third color. Nodes are colored differently depending on how many circuit elements are connected to them (i.e., a node connected to two elements will have a different color than one connected to three elements). In this sense, if

two circuits are equivalent up to a swap of components or vertices, then there exists an isomorphism between their component graph representations. Graph isomorphism is a computationally difficult problem, but we consider sufficiently small graphs for the technique to remain feasible. Component graph isomorphism is used extensively by Herber et al. in their treatment of classical circuit enumeration [5, 6].

In Fig. 4, we show that two Y circuits are isomorphic using this component graph formalism. The two circuits are clearly equivalent up to a 120° rotation of their circuit diagrams. In our software implementation of the isomorphism reduction, we begin with the first circuit in our database. Subsequent circuits are compared with each existing element in the set, and if no isomorphism exists, it is added to the non-isomorphic set. This process is repeated for each selection of circuits that contain a fixed number of components (i.e., 2 C, 1 L, 1 J), as this is required for component-like isomorphism.

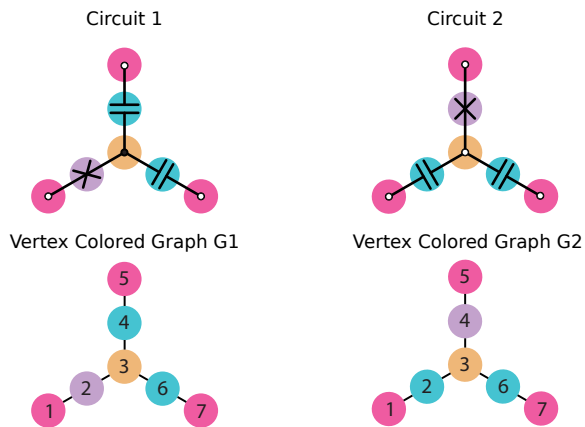


FIG. 4. Two equivalent circuits (top), along with their component graph representations (bottom). Each circuit component and node in the circuit diagram is represented by a colored vertex. Different circuit components are assigned different colors (capacitor \rightarrow blue, Josephson junction \rightarrow purple). Each node in the circuit is assigned a color based on its degree (1 connection \rightarrow pink, 3 connections \rightarrow orange). An isomorphism exists from $G_1 \rightarrow G_2$ with vertex mapping $\{1 \rightarrow 5, 2 \rightarrow 4, 3 \rightarrow 3, 4 \rightarrow 2, 5 \rightarrow 1, 6 \rightarrow 6, 7 \rightarrow 7\}$.

IV. TOWARDS HAMILTONIAN ENUMERATION AND REDUCTION

Unique circuits do not always correspond to unique behaviors. To address this issue, we present progress towards a “Hamiltonian enumeration” and a “Hamiltonian reduction” step. The goal here is to refine the classical enumeration results and produce a set of “unique” Hamiltonians. These steps are based on circuit quantization and the reduction involves categorizing Hamiltonians by the types of operators present. To enumerate Hamiltonians, we take the circuits generated by the enumeration

algorithm and follow the standard circuit quantization procedure [69–74].

The issue of different circuits leading to identical circuit function also occurs in classical circuit theory. For example, the two LC circuits in Fig. 5 have different topologies but can have equal impedance with $(C_1, C_2, L_1) = (6C, 3C, L/9)$ [75]. This equivalence can be beneficial. For example, if a large inductor is hard to manufacture, an alternative circuit with the same electrical properties might be easier to build. For instance, circuit (b) requires a nine times smaller inductor to achieve the same impedance as circuit (a).

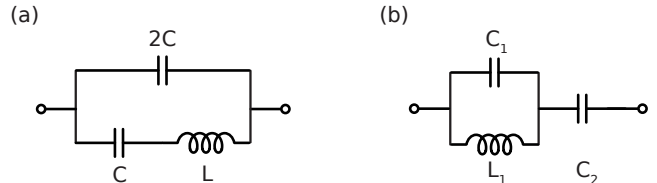


FIG. 5. Circuits with equivalent impedance across the outer ports in the case $(C_1, C_2, L_1) = (6C, 3C, L/9)$.

Trying to find exact equivalences between nonlinear Hamiltonians is difficult. Instead, we take a different approach that involves counting and categorizing the operators present in the Hamiltonian. In superconducting qubits, operators in a multimode Hamiltonian can be divided into harmonic, extended, and periodic modes, see Fig. 6 and Ref. [8]. We aim to identify circuits with Hamiltonians that have the same types and numbers of modes, along with similar nonlinear terms and inter-mode couplings.

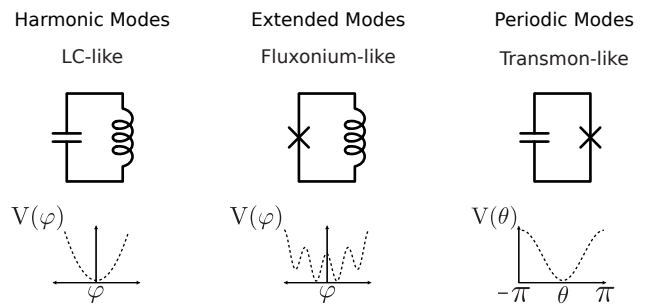


FIG. 6. Types of variables present in nonlinear superconducting circuits. Here and throughout we will denote harmonic and extended modes using q, φ and periodic modes using n, θ .

We say that two circuits are in the same “class” if their Hamiltonians contain the same set of operators, up to a change of variables. Of course, circuits within the same class can differ greatly. For instance, the Cooper pair box and transmon qubits share a single periodic mode, but the transmon is less sensitive to charge noise due to its larger E_J/E_C ratio. It is worth noting that in the circuit quantization, we consider a small parasitic capacitance in parallel with each Josephson junction. Two circuits that

differ by a shunting capacitor across a junction will therefore be in the same Hamiltonian class. However the circuit properties will ultimately depend on coefficients that are functions of the physical capacitance, inductance, and Josephson energies.

In general, to show two Hamiltonians are in the same class, a variable transformation must align the operators in the Hamiltonians. No general method exists to find such a transformation, but verifying one is straightforward. We use the `scQubits` python package to suggest a transformation which both removes non-dynamical variables and separates periodic from harmonic and extended variables through simple coordinate changes [8]. This variable transformation does not depend on the underlying circuit parameters, which gives each circuit a single Hamiltonian to compare to others.

Here the Hamiltonian enumeration consists of quantizing each unique circuit, while the Hamiltonian reduction involves sorting the resulting expressions into classes. Similarly to the reduction step of the circuit enumeration algorithm, we build the Hamiltonian classes through a series of pairwise comparisons. To be clear, our procedure examines a circuit’s Hamiltonian using the suggested transformation; it does not determine whether there exists a transformation that brings that circuit into a particular Hamiltonian class. It is likely that some classes are equivalent under a secondary transformation of variables.

Within our Hamiltonian reduction, we consider two separate cases. In the general case, we allow all underlying circuit components to vary independently (i.e., capacitors have capacitance C_1, C_2, \dots, C_n). In the “symmetric” case we give identical properties to each type of component (i.e., all capacitors have capacitance C and all inductors have inductance L). Some circuits, such as the $0-\pi$ qubit, leverage identical C , L , and E_J to remove unwanted inter-mode coupling terms [56]. Identical parameters represent a special case where some operators may disappear, potentially splitting a single class in the general class into many classes in the symmetric case.

V. ENUMERATION RESULTS

Here we present the results of our circuit enumeration, along with our progress towards Hamiltonian enumeration and reduction. There are many subtleties in producing the Hamiltonians for our enumerated circuits, and we briefly discuss some of these challenges in appendix A.

The source code that implements the circuit enumeration, circuit reduction and Hamiltonian reduction can be found at the following Git repository [76]. It is possible to complete the full procedure for up to four nodes using a standard computer, but five nodes requires a cluster or large server. To enumerate the five node circuits and Hamiltonians, we used about 50,000 core hours on a server with dual AMD EPYC 7713 processors with 2TB of RAM.

A. Number of Circuits & Hamiltonian Classes

We present three tables that summarize our enumeration results. The first table, table I, shows information as a function of the number of nodes. The large numbers in the second column show combinatorial explosion of the number of circuits. In the third column, we bring to bear the circuit reduction steps from Sec. III B. The number of unique circuits is significantly smaller than the total number of circuits.

In the fourth column “classes” refers to the number of Hamiltonians after quantizing all circuits and performing Hamiltonian reduction, as detailed in Sec. IV. The two node Hamiltonian classes are $n^2 + \cos(\theta)$ and $q^2 + \varphi^2 + \cos(\varphi)$, representing a single periodic mode (transmon-like) and extended mode (fluxonium-like) respectively. For larger circuits, the listed number of discovered Hamiltonian classes is an upper bound on the true number of Hamiltonian classes, as some may be equivalent under secondary transformations. Nevertheless, we find many orders of magnitude fewer Hamiltonian classes than there are unique circuits.

In the fifth column, we consider the “symmetric” case of Hamiltonian reduction, where all like circuit elements are considered identical. This special case where terms may disappear is denoted by “Sym” for symmetric. We see that the number of additional Hamiltonian classes unlocked by identical circuit parameters grows with the size of the circuit and only appear for those larger than three nodes. This increase may stem from additional four and five node circuit topologies that exhibit different symmetries than those found in smaller circuits.

The other two tables, table II and table III, separate the number of unique circuits and Hamiltonian classes by the number of JJs or the number of flux loops in a given circuit. For example, there are 2594 unique four node circuits that contain two junctions. This includes the $0 - \pi$ [56] and the Dfluxmon [62] qubits. They are both derived from the fully connected 4 node base graph topology (see Fig. 3), which can alternatively be drawn as a triangle with an additional interior node.

In both tables, the sum of column 4 (number of Hamiltonian classes) over a particular node can be larger than the corresponding value in table I. This imbalance shows that circuits with different numbers of junctions and flux loops can be in the same Hamiltonian class, although there are far more examples with different numbers of flux loops. Curiously, in the symmetric case, we see no Hamiltonian classes that contain circuits with different numbers of junctions. In this case, the sum of column 5 over a specific node, but not column 4, in table II matches table I. The $0-\pi$ qubit, which contains two JJs, is one such example. In the case of unequal underlying E_J , it gets placed in the same Hamiltonian class as some circuits that only contain a single junction.

The ultimate goal of our circuit enumeration is to assist with circuit design or optimization problems. Unsurprisingly, we observe that adding or subtracting a Josephson

Nodes	Circuits	Unique Circuits	Classes	Classes (Sym)
2	7	4	2	2
3	392	88	22	22
4	139,944	11,614	165	298
5*	338,332,113	498,161	3546	10294

TABLE I. Number of enumerated circuits and Hamiltonian classes as a function of number of nodes in the circuit. Column 1 is the number of nodes in a circuit. Column 2 is the naive estimate of the number of circuits 7^{N_E} for a given number of nodes, summed over all base graphs (see Fig. 3). For three node circuits, we sum over two base graphs thus $7^3 + 7^2 = 392$. Column 3 is the number of unique circuits that include at least one Josephson junction. There are many equivalent circuits in the naive estimate, so a huge reduction is observed between columns 2 and 3. Column 4 is the number of Hamiltonian classes identified from the set of unique circuits, which serves as an upper bound on the number of classes present. The two node Hamiltonian classes are $q^2 + \cos(\theta)$ and $q^2 + \varphi^2 + \cos(\varphi)$, representing a transmon and fluxonium respectively. There are four unique circuits because the junction can be explicitly shunted by an additional capacitor in both cases. Column 5 reports the number of Hamiltonian classes present for the same transformation, fixing all elements of the same type to have equivalent values. For circuits such as the $0-\pi$ qubit, this represents a special case where certain coefficients go to zero. *In the 5 node case we only use five elements {C, J, L, CL, JL}. If parasitic capacitance is considered for Josephson Junctions, the number of Hamiltonian classes is the same as for the seven elements {C, J, L, CL, JL, CJ, CJL}. Using only 5 elements greatly reduces the number of unique circuits, making the analysis of five node circuits feasible.

junction from a circuit constitutes a meaningful change in the Hamiltonian. However, there do exist many circuits with similar Hamiltonians but different numbers of flux loops. Circuits with fewer loops would likely be easier to build, although it is possible that these additional loops could offer valuable control knobs at the expense of complexity. A benefit of our reduction procedure is that both physically equivalent circuits and those within the same Hamiltonian class can be obtained straightforwardly after the fact. Because all possible configurations are considered, the task of generating a set of equivalent circuits becomes a simple database search.

B. Equivalent Circuits and Hamiltonians

Circuits can be equivalent or function similarly despite differences in their physical layouts. One application of our enumeration is to, for a specific circuit, produce all equivalent diagrams. For small circuits like the three node Δ configuration shown in Fig. 2, equivalent diagrams are largely trivial rotations or reflections. For more complicated topologies, non-obvious equivalent circuits are identified by our reduction procedure.

We are similarly able to identify circuits that are not

Nodes	JJs	Unique Circuits	Classes	Classes (Sym)
2	1	4	2	2
3	1	28	8	8
	2	40	10	10
	3	20	4	4
4	1	968	18	29
	2	2594	57	84
	3	3708	58	80
	4	2852	34	60
	5	1216	12	25
	6	276	7	20
5*	1	40192	111	196
	2	94786	449	969
	3	130910	653	1410
	4	117614	972	2565
	5	72120	882	2305
	6	30933	569	1664
	7	9320	257	807
	8	1956	90	288
	9	296	29	72
	10	34	10	18

TABLE II. Number of unique circuits and Hamiltonian classes split by number of nodes and Josephson junctions. Circuits with different numbers of Josephson junctions are never in the same Hamiltonian class when all underlying circuit parameters are identical (column 5), but occasionally are in the same Hamiltonian class when parameters are allowed to vary (column 4). *In the 5 node case we only use five elements {C, J, L, CL, JL}, while in the 2/3/4 node circuits we also include {CJ, CJL}.

equivalent diagrams but realize Hamiltonians of the same class. We call such systems “copycat” circuits. Importantly, these “copycat” circuits may realize the specific Hamiltonian in a different parameter regime. We will take as an example the $0-\pi$ qubit (shown in Fig. 7 (a)), which has the Hamiltonian

$$H_{0-\pi} = E_{C1}n_1^2 + E_{C2}q_2^2 + E_L\varphi_2^2 - 2E_J \cos \theta_1 \cos \varphi_2 \quad (2)$$

in the case where each pair of underlying capacitors, inductors, and Josephson junctions are identical. Note there is an additional uncoupled harmonic third mode not shown. In order for the qubit to be protected, it is important that E_L is small, E_{C1}/E_J is small, and E_{C2}/L is large [77]. The standard circuit that implements this Hamiltonian is shown in Fig. 7(a). From our enumeration procedure, we find one distinct inductive circuit that realizes this Hamiltonian form, with many different choices for placement of capacitors. These options are also shown in Fig. 7(a). The primary difference between these Hamiltonians is the way in which the underlying capacitance are expressed in E_{C1} and E_{C2} . Depending on the capacitive circuit chosen, they differ in whether the periodic or extended modes are light or heavy respectively. Out of all these combinations, only the original $0-\pi$ circuit has small E_{C1} (heavy) and large E_{C2} (light).

The $0-\pi$ circuit has a high degree of symmetry, so

Nodes	Loops	Unique Circuits	Classes	Classes (Sym)	
2	0	2	1	1	
	1	2	1	1	
3	0	16	5	5	
	1	32	9	9	
	2	24	8	8	
	3	12	4	4	
	4	4	1	1	
4	0	440	25	26	
	1	1369	52	65	
	2	2268	72	100	
	3	2683	62	96	
	4	2334	35	69	
	5	1503	20	48	
	6	712	6	26	
	7	238	3	14	
	8	56	1	5	
	9	11	1	3	
	5*	0	6382	184	226
		1	24537	567	817
		2	51011	1053	1774
		3	77552	1361	2579
		4	92579	1228	3144
		5	89236	819	3150
6		70408	502	2786	
7		45673	296	2150	
8		24454	181	1505	
9		10803	94	877	
10		3939	53	472	
11		1192	29	211	
12		309	17	84	
13		68	6	25	
14		14	4	8	
15		3	2	2	
16	1	1	1		

TABLE III. Number of unique circuits and Hamiltonian classes split by number of flux loops in the circuit. Many circuits with different numbers of flux loops are in the same Hamiltonian class. *In the 5 node case we only use five elements $\{C, J, L, CL, JL\}$, while in the 2/3/4 node circuits we also include $\{CJ, CJL\}$.

it is perhaps unsurprising that there are no nontrivial equivalent circuits, and only one unique inductive circuit that realizes the Hamiltonian class. Here inductive circuit means the circuit formed out of only inductors and Josephson junctions. For a more expansive example, we consider the Difluxmon circuit [62]. As seen in Fig. 8, the Difluxmon has the same circuit topology as $0-\pi$, with one inductor and capacitor swapped. There are two nontrivial equivalent circuits identified using our reduction procedure, plus an additional nine trivial rotations and reflections. We find seven unique inductive circuits in the same Hamiltonian class, containing 120 unique circuit diagrams. Many have similar dependence on physical parameters as the original circuit, hinting that they could be equivalent with an appropriate choice of the underlying circuit parameters. It is possible that some of these

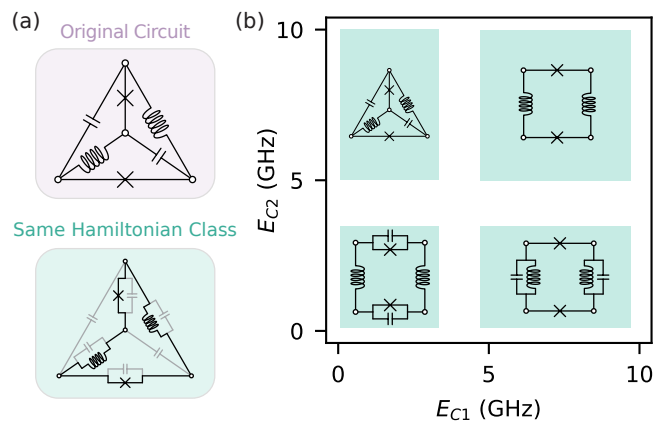


FIG. 7. (a) The original $0-\pi$ circuit and all “copycat” circuits in the same Hamiltonian class. For the specified $0-\pi$ Hamiltonian, capacitors shown in gray must be included or excluded in pairs across identical elements to maintain the appropriate symmetry. (b) Parameter regions accessible for each choice of capacitive circuit, assuming junction capacitance of 5-10 GHz and capacitor capacitance of 0.05-5 GHz. Each circuit shown represents a choice to include one or none of the specified gray pairs of capacitors in (a). All circuits with multiple pairs of capacitors fall in the bottom left region. Only the original $0-\pi$ circuit (top left) has a heavy periodic mode and light extended mode by virtue of including the lone capacitor but excluding shunting capacitors on both the inductors and junctions.

circuits may be easier to fabricate, or may offer other practical advantages.

C. Hamiltonian Enumeration

In addition to identifying equivalent circuits and Hamiltonians, we can use the results of our enumeration to investigate the structure of Hamiltonian classes in general. We call this process “Hamiltonian enumeration.” To illustrate the concept, we show all Hamiltonian classes corresponding to two and three node circuits in table IV. Recall that we categorize Hamiltonians based on the number of periodic, extended, or harmonic modes, plus their nonlinearities and inter-mode coupling. Coefficients and their dependence on physical parameters are removed for space, but they are recorded in the enumeration procedure, and instructions on how to retrieve them are provided on our Github repository [76]. The corresponding table for four nodes (which includes the $0-\pi$ and Difluxmon circuits detailed in the previous section) is included as a separate PDF and tex document in the arXiv source file (e.g. `results_table_4node.pdf`), while the five node results are included as a series of six tex documents due to the number of classes present (e.g. `results_table_5node_0per.tex`).

Columns one and two uniquely identify the Hamiltonian class by the number of nodes in the circuit and an additional class index. These numbers are used to label

Nodes	Class	Hamiltonian Form	Periodic	Extended	Harmonic	#Circuits
2	1	$n_1^2 + \cos \theta_1$	1	0	0	2
	2	$q_1^2 + \varphi_1^2 + \cos \varphi_1$	0	1	0	2
3	1	$n_1^2 + \cos \theta_1$	1	0	0	4
	2	$n_1^2 + q_2^2 + \varphi_2^2 + \cos \theta_1$	1	0	1	2
	3	$n_1^2 + n_1 q_2 + q_2^2 + \varphi_2^2 + \cos \theta_1$	1	0	1	4
	4	$q_1^2 + \varphi_1^2 + \cos \varphi_1$	0	1	0	4
	5	$q_1^2 + q_2^2 + \varphi_1^2 + \varphi_2^2 + \cos \varphi_2$	0	1	1	2
	6	$q_1^2 + q_1 q_2 + q_2^2 + \varphi_1^2 + \varphi_2^2 + \cos \varphi_2$	0	1	1	4
	7	$q_1^2 + q_2^2 + \varphi_1^2 + \varphi_1 \varphi_2 + \varphi_2^2 + \cos \varphi_2$	0	1	1	4
	8	$q_1^2 + q_1 q_2 + q_2^2 + \varphi_1^2 + \varphi_1 \varphi_2 + \varphi_2^2 + \cos \varphi_2$	0	1	1	4
	9	$n_1^2 + n_2^2 + \cos \theta_1 + \cos \theta_2$	2	0	0	3
	10	$n_1^2 + n_1 n_2 + n_2^2 + \cos \theta_1 + \cos \theta_2$	2	0	0	3
	11	$q_1^2 + q_2^2 + \varphi_1^2 + \varphi_2^2 + \cos \varphi_1 + \cos \varphi_2$	0	2	0	3
	12	$q_1^2 + q_1 q_2 + q_2^2 + \varphi_1^2 + \varphi_2^2 + \cos \varphi_1 + \cos \varphi_2$	0	2	0	3
	13	$q_1^2 + q_2^2 + \varphi_1^2 + \varphi_1 \varphi_2 + \varphi_2^2 + \cos \varphi_1 + \cos \varphi_2$	0	2	0	5
	14	$q_1^2 + q_1 q_2 + q_2^2 + \varphi_1^2 + \varphi_1 \varphi_2 + \varphi_2^2 + \cos \varphi_1 + \cos \varphi_2$	0	2	0	5
	15	$n_1^2 + q_2^2 + \varphi_2^2 + \cos \theta_1 + \cos \varphi_2$	1	1	0	4
	16	$n_1^2 + n_1 q_2 + q_2^2 + \varphi_2^2 + \cos \theta_1 + \cos \varphi_2$	1	1	0	4
	17	$n_1^2 + n_1 n_2 + n_2^2 + \sin \theta_1 \sin \theta_2 + \cos \theta_1 \cos \theta_2 + \cos \theta_1 + \cos \theta_2$	2	0	0	4
	18	$n_1^2 + n_1 q_2 + q_2^2 + \varphi_2^2 + \sin \theta_1 \sin \varphi_2 + \cos \theta_1 \cos \varphi_2 + \cos \theta_1$	1	1	0	6
	19	$q_1^2 + q_1 q_2 + q_2^2 + \varphi_1^2 + \varphi_2^2 + \sin \varphi_1 \sin \varphi_2 + \cos \varphi_1 \cos \varphi_2 + \cos \varphi_2$	0	2	0	4
	20	$q_1^2 + q_1 q_2 + q_2^2 + \varphi_1^2 + \varphi_2^2 + \sin \varphi_1 \sin \varphi_2 + \cos \varphi_1 \cos \varphi_2 + \cos \varphi_1 + \cos \varphi_2$	0	2	0	4
	21	$q_1^2 + q_1 q_2 + q_2^2 + \varphi_1^2 + \varphi_1 \varphi_2 + \varphi_2^2 + \sin \varphi_1 \sin \varphi_2 + \cos \varphi_1 \cos \varphi_2 + \cos \varphi_1 + \cos \varphi_2$	0	2	0	6
	22	$n_1^2 + n_1 q_2 + q_2^2 + \varphi_2^2 + \sin \theta_1 \sin \varphi_2 + \cos \theta_1 \cos \varphi_2 + \cos \theta_1 + \cos \varphi_2$	1	1	0	6

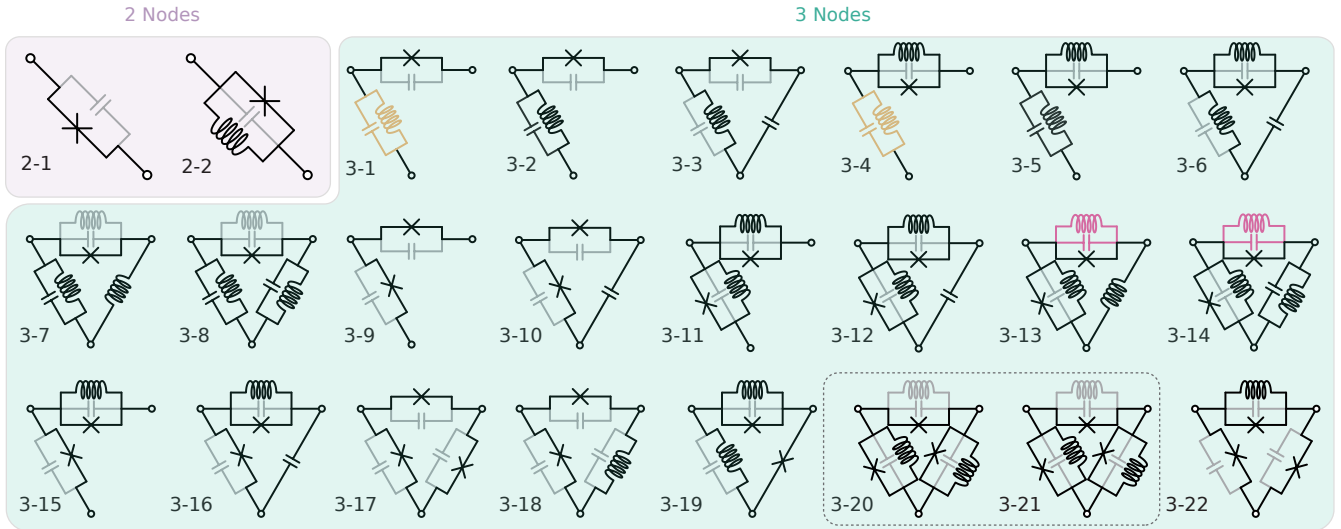


TABLE IV. Identified Hamiltonian classes (top) and corresponding circuits (bottom) up to 3 nodes in size. Coefficients are omitted for space, although they are present in the database. Periodic variables are denoted by n, θ , while extended and harmonic variables are denoted by q, φ . Grayed out circuit elements may be removed without changing the Hamiltonian class. Circuits with orange elements must have exactly one of the two highlighted elements, while those with pink elements must have at least one of the two highlighted elements. The circuits for classes 3-20 and 3-21 cannot be drawn distinctly from each other. The two classes contain diagrams that differ only by capacitors across Josephson junctions, indicating that under a different transformation of variables, they would be in the same class.

the circuits below the table, which each correspond to an individual Hamiltonian class. Column three shows the Hamiltonian class, with operator coefficients removed. Here periodic variables are denoted by n, θ , while ex-

tended and harmonic variables are denoted by q, φ . The columns on the right indicate the number of periodic, extended, and harmonic modes (see Fig. 6 for a description of these modes). For the circuit diagrams below the ta-

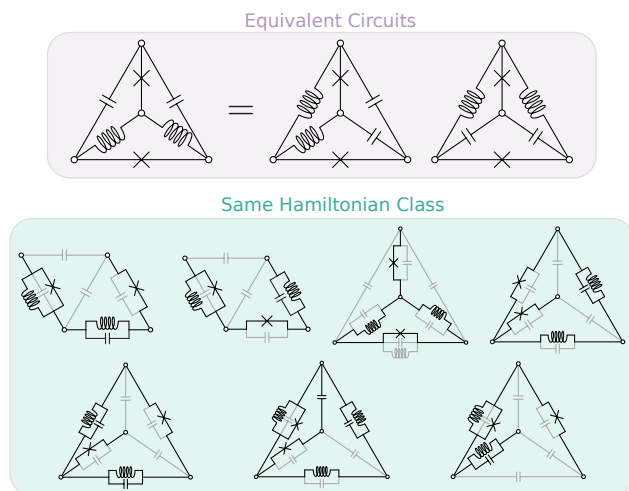


FIG. 8. (Top) Circuits equivalent to the Difluxmon circuit [62]. For each diagram shown, there are three trivial rotations, plus a reflection across the top junction for the middle diagram, making 12 total configurations. (Bottom) All circuits in the same Hamiltonian class as the original Difluxmon circuit. Unique inductive circuits are shown separately, with gray elements representing those that can be added or subtracted without changing the Hamiltonian class. Unlike the elements in Fig. 7 these gray elements may be added and removed individually.

ble, gray elements on the circuit diagram can be removed without changing the Hamiltonian class. Pairs of orange elements indicate that exactly one of the two must be in the circuit, and pairs of pink elements indicate that at least one of the two must be present.

As stated earlier, the two node circuits are either fluxonium-like (a single extended mode) or transmon-like (a single periodic mode). For three node circuits, there are 22 classes of Hamiltonians. These circuits only have two modes, so no three-node circuit contains all three kinds of modes. Most (classes 1-16) can be understood as either individual or charge/flux coupled transmon, fluxonium, and resonator circuits. Indeed they have the expected circuits, with most variation being optional capacitors. Classes 17-22 exhibit nonlinear coupling of the underlying modes. These classes contain all circuits with three Josephson junctions, plus a fluxonium inductively coupled to a transmon. Still, most variation in the underlying circuits is again down to optional capacitors. To see Hamiltonian classes with substantially different topologies or inductive circuits, four nodes are required (for example the Difluxmon circuit in Fig. 7).

The structure of table IV also highlights some of the limitations of our current Hamiltonian enumeration and reduction procedure. For example, two different sets of classes ($\{3 - 13, 3 - 14, 3 - 9\}$ and $\{3 - 20, 3 - 21\}$) contain diagrams that differ only by capacitors across Josephson junctions. Because we explicitly consider a small capacitance across the junction, these circuits must be in the same class under a different variable transform-

ation. Indeed the circuits contained by classes 3 – 20 and 3 – 21 cannot be drawn distinctly using the gray, orange, and pink rules outlined in table IV.

In table III, we saw that at most five different three node Hamiltonian classes contain circuits with different numbers of flux loops. Looking at table IV, we see that these are classes 7, 8, 13, 14, and 21, for which adding an additional inductor to a branch with a Josephson junction does not change the Hamiltonian class. In each of these cases, the circuit already has two inductors and two non-periodic modes. Indeed, each inductor in the three node circuits (up to the number of modes present – two) appears to correspond to an extended or harmonic mode in the Hamiltonian. Conversely, a Josephson junction without an accompanying inductor is required for a periodic mode.

The three node case can provide intuition for the relative abundance of extended/harmonic modes relative to periodic modes, although larger circuits may not obey such simple rules. Of the three node Hamiltonian classes, over half have no periodic modes, while only three classes have periodic modes only. Similar statements are true for larger circuits, suggesting that periodic modes are less abundant in the landscape of superconducting circuit Hamiltonians. As seen in table V, periodic modes become more scarce, in terms of unique circuits, as the size of the circuits increase. Indeed 50%, 45%, 38%, and 25% of unique circuits with 2, 3, 4, and 5 nodes contain at least one periodic mode. Conversely, the share of Hamiltonian classes containing at least one periodic variable grows with the number of nodes.

Nodes	Periodic	Unique Circuits	Classes	Classes (Sym)
2	0	2	1	1
	1	2	1	1
3	0	48	12	12
	1	30	7	7
	2	10	3	3
4	0	7216	37	137
	1	3298	80	112
	2	942	38	39
	3	158	10	10
5*	0	372254	627	5219
	1	102177	1204	2958
	2	20537	1328	1718
	3	2939	332	344
	4	254	55	55

TABLE V. Number of unique circuits and Hamiltonian classes present for circuits with the specified number of nodes and periodic variables. Circuits with periodic variables become increasingly more scarce as circuits get larger, although the fraction of Hamiltonian classes with periodic variables remain consistent. *In the 5 node case we only use five elements $\{C, J, L, CL, JL\}$, while in the 2/3/4 node circuits we also include $\{CJ, CJL\}$.

VI. OPTIMIZING CIRCUIT PERFORMANCE

As a precursor to searching over all three node circuits, we develop a framework that will enable us to numerically optimize the parameters of a particular circuit. Then in the next section Sec. VII, we will use this machinery to search for new qubits by explicitly considering all possible three-node circuits.

In this section, we estimate and then optimize the number of gates possible within a circuit’s coherence time, with respect to the underlying circuit parameters. No element of this procedure is specific to the problem of qubit discovery. We then validate our algorithm on the well-studied transmon and fluxonium qubits.

A. Objective Function and Optimization

Any of the circuits generated in Sec. III could be used as a superconducting qubit, but we expect some to perform much better than others. We choose to rank circuits by an estimate of the number of gates that can be performed within coherence time t_2

$$N_{\text{gate}} = \frac{t_2}{t_{\text{gate}}}. \quad (3)$$

Here t_{gate} is an estimate of the length of a single qubit gate. We choose to use $t_2 = 1/2t_1 + 1/t_\phi$ to include the effects of both energy relaxation t_1 and dephasing t_ϕ . Due to the many assumptions made in estimating t_2 and t_{gate} , N_{gate} is ultimately a qualitative metric. In other words, the relative values between different circuit configurations is more meaningful than the exact value.

To determine t_2 , we use the `SQcircuit` package to analyze our circuits [12, 63]. In our work we consider the three depolarization and three dephasing channels supported by the package. Depolarization rates are calculated using Fermi’s golden rule, while dephasing rates depend on the sensitivity of the qubit frequency ω_0 to noise parameters. We use the default noise amplitudes, which agree with the lower bound presented in [78]. For more details on how these rates are calculated, see [12, 63].

To estimate t_{gate} , we consider a simplified three level system and estimate the time necessary to complete either a direct transition $|0\rangle \rightarrow |1\rangle$ or a transition via the higher lying state $|0\rangle \rightarrow |2\rangle \rightarrow |1\rangle$. Our model, detailed in appendix B, considers both leakage out of the computational subspace and implements a maximum drive constraint. It is worth noting that our procedure does not consider the matrix elements and coupling required to drive these transitions. It is purely based on the frequency differences between the first three states. For larger circuits, driving the gate could require complicated multi-node schemes. In appendix C we detail additional important assumptions in our modeling.

We now face the problem of optimizing Eq. (3), with respect to the underlying parameters of a circuit. The number of dimensions in the optimization problem is equal

to the number of circuit elements, plus the number of offset charges or flux biases present in the system. We use a python implementation of the differential evolution algorithm [79] to perform this optimization. Differential evolution is a widely used genetic algorithm that does not require the gradient of the objective function. At a high level, differential evolution works by maintaining a population of agents that exist at different points in the space being optimized. These agents are combined or “mutated” to reach new points, with the best performers included in a new generation of agents. This process is repeated until the agents converge (or a maximum number of iterations is reached).

B. Parameter Ranges

A key choice in the optimization procedure is a range of parameter values for the individual underlying circuit elements. For the rest of this paper, we work with parameter values in frequency units: E_C , E_L , and E_J . We choose parameter ranges that include slightly larger capacitors and inductors than those seen in superconducting qubits today, in the hope that design and materials advances will enable such devices. We choose not to include very small inductors in our search range.

Parameter	Min (Freq)	Max (Freq)	Min (SI)	Max(SI)
E_C, C	0.05 GHz	10.0 GHz	1.9 fF	0.39 pF
E_L, L	0.05 GHz	5.0 GHz	33 nH	3.3 μ H
E_J, L_J	1.0 GHz	30.0 GHz	5.4 nH	0.16 μ H
E_{C_J}, C_J	10.0 GHz	10.0 GHz	1.9 fF	1.9 fF

TABLE VI. Ranges for underlying circuit parameters used in the optimization problem. The junction capacitance C_J is taken to be fixed, as the smallest capacitance allowed for dedicated capacitors. For details on how to convert between these units and physical capacitance/inductance, see appendix D.

C. Comparing Model With Published Results

To validate our model of qubit performance, we compare our predicted optimal operating points for the transmon and fluxonium qubits with published experimental values. Including charge offset n_g and external flux φ_{ext} , the Hamiltonians for the two systems are

$$H_{\text{Transmon}} = 4E_C(n - n_g)^2 - E_J \cos(\theta) \quad (4)$$

$$H_{\text{Fluxonium}} = 4E_Cq^2 + \frac{1}{2}E_L\varphi^2 - E_J \cos(\varphi - \varphi_{\text{ext}}). \quad (5)$$

Due to the limited number of parameters involved in these circuits, we visualize N_{gate} as a 2D parameter sweep in Fig. 9. In the case of fluxonium, E_C is fixed at 500 MHz, with E_L and E_J expressed in units of E_C . For

the transmon, $n_g = 0.25$ is chosen to represent a worst case offset when a DC offset is not included. For fluxonium, the standard $\varphi_{\text{ext}} = \pi$ is used. To provide a fair comparison with the published experimental values, we restrict our parameter ranges slightly (relative to the ranges in table VI), considering capacitors and inductors of $E_C/E_L \geq 0.1$ GHz. Qubits from the literature fall near or within the best-performing regions for both the transmon and fluxonium circuits.

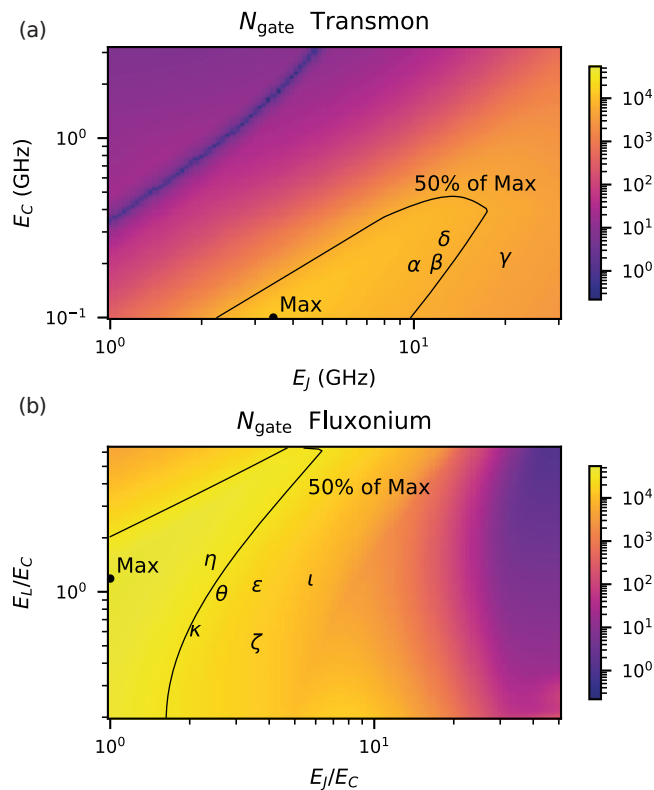


FIG. 9. Qualitative estimate of N_{gate} calculated for the transmon (a) and fluxonium (b) Hamiltonians shown in Eq. (4). For the transmon, $n_g = 0.25$ is chosen to represent a worst case offset when a DC offset is not included. For fluxonium, the standard $\varphi_{\text{ext}} = \pi$ is used. The black dot marks the maximum point, and the black contour shows the region that is at least 50% of the maximum value. The maximum value of N_{gate} is approximately 12,500 for the transmon and 54,500 for fluxonium. These numbers are qualitative so the value of the maximum is less important than relative values. The streak with low N_{gate} for the transmon is due to a zero crossing of the anharmonicity (positive anharmonicity in the top left negative anharmonicity in the bottom right). It is important to note that our gate time model is crude, and noise models may not match experiments. To gauge the discrepancies between our model and experimental data, we extracted the circuit parameters from various published qubit designs. Each letter corresponds to parameters from a published paper: transmon α –[50], β –[80], γ –[81], and δ –[82]; fluxonium ϵ –[83], ζ –[84], η –[85], θ –[86], ι –[87], and κ –[88]. Qubits from the literature fall near or within the best performing regions for both the transmon and fluxonium circuits.

In Fig. 9 (a) it is evident that transmon from the literature fall close to the contour 50% of the numerically optimal point. The agreement is remarkable, perhaps reflecting that noise in the transmon is well understood. The discrepancy could be explained by the fact that our optimization doesn’t account for coupling to readout resonators, Purcell filters, device size or many other important practical considerations. Readers wishing to understand the interplay between the number of gates estimate and the noise models should consult appendix E, where we have the parameter sweeps for all the noise models. In summary, the agreement between our naive numerical model and real-world data builds confidence in the metrics we will use to optimize unknown circuits.

In the case of Fluxonium, shown in Fig. 9 (b), fewer of the published experiments fall within 50% of our numerically optimized point. There are several possible explanations for this disagreement. The most likely is the noise model for fluxonium is less accurate, although it is also possible that fluxonium is simply less studied than the transmon. Nevertheless, all points except ι fall above 25% of the maximum value. The agreement is still (in our opinion) impressive, considering neither the noise nor gate speed models have been fine tuned for fluxonium.

D. Algorithmically Optimized Fluxonium

Finally we wish to test our full optimization algorithm by seeing if our model can discover a new operating point in fluxonium. Here we allow the algorithm to additionally pick E_C and φ_{ext} , as compared with the parameter sweeps in the previous section. The algorithm identified $E_C = 3.69$ GHz, $E_J = 5.93$ GHz, $E_L = 0.100$ GHz, and $\varphi_{\text{ext}} = 0$ as the optimal point, corresponding to $N_{\text{gate}} \approx 108,000$. It is important to note that N_{gate} is a qualitative estimate. To be clear, we do not expect a fluxonium built with these parameters to be capable of running over 100,000 gates. Here the relative values and position of the maximum is most important.

In Fig. 10, we show the energy spectrum and wave functions for the optimized fluxonium. The system appears similar to the recently proposed “Integer Fluxonium” qubit, for which $|0\rangle$ is found mostly in the central well, and $|1\rangle$ and $|2\rangle$ are largely in a superposition of the wells at $\varphi = -\pi, \pi$ [89]. Our optimized fluxonium appears as a “light” version of the integer fluxonium. Similar to a light vs. heavy fluxonium, the wavefunctions of the optimized circuit are less localized and the flux dispersion is less steep. It is worth noting that neither of these systems appear in Fig. 9, as they have a different value for φ_{ext} .

Comparing our optimized point with integer fluxonium also illustrates a limitation with the gate time estimates in our procedure. In integer fluxonium, the $|0\rangle \rightarrow |2\rangle$ transition is forbidden by parity, an important factor that does not appear explicitly in our model. This has particular ramifications for the gate speed estimate, as direct

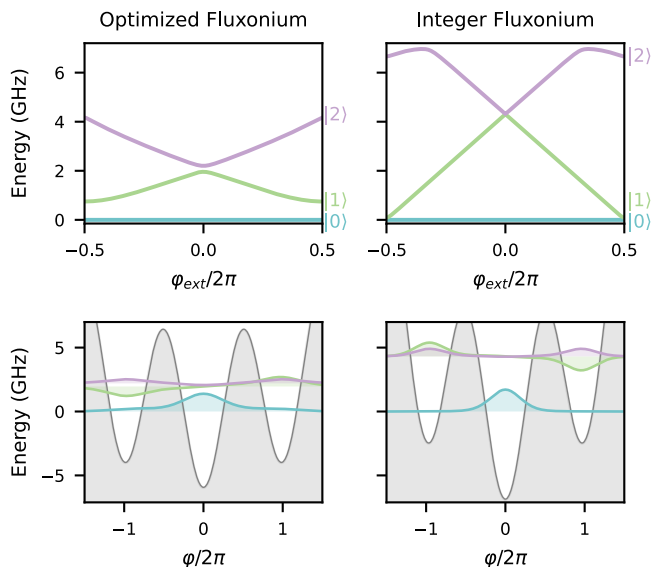


FIG. 10. Dependence of the first three energy levels on external flux (top), of optimized fluxonium (left) and Integer fluxonium (right), using parameters from [89]. The first three eigenstates are plotted for both circuits (bottom), with global phase calibrated to make the peak value of the $|0\rangle$ state positive.

transitions $|0\rangle \rightarrow |1\rangle$ can be thus be driven faster than would be expected from the nearly degenerate $|1\rangle$, $|2\rangle$ states. Our optimization procedure, however, was still able to identify a similar system that did not rely explicitly on these selection rules.

VII. SEARCHING FOR NEW QUBITS

We now apply the optimization methods detailed in Sec. VI to the 4 unique two node circuits and 88 unique three node circuits. The goal here is to find a good superconducting qubit, as judged by N_{gate} . We again remind the reader that that statements about N_{gate} are qualitative, so the absolute value of N_{gate} for a particular circuit is less important than the value relative to other circuits.

In considering large numbers of unstudied circuits, we are forced to make key assumptions in how the systems are modeled. One choice with potentially large implications is assigning a ground node. Rather than explicitly grounding one of the three nodes, we consider weak capacitive coupling to ground from each node. In appendix C, we show further details of our modeling, including our approach to selecting computational states, determining a hilbert space cutoff, setting $1/f$ noise amplitudes, optimizing external offsets, and coupling to the circuits.

After optimizing each circuit, we perform a sensitivity analysis to highlight circuits that are robust to small changes in the optimized circuit parameters (modeling small fabrication imperfections). This analysis is done

by randomly sampling 100 nearby points in parameter space, using a Normal distribution with 2.5% standard deviation around the optimized value. The tables that follow will show the mean and standard deviation of these 100 points. Good candidate qubits have low variance relative to the average value.

To produce the results in this section, we used about 30,000 core hours on a server with dual AMD EPYC 7713 processors and 2 TB of RAM. The vast majority of this time was spent on circuits with two extended modes, as these require far higher Hilbert space cutoffs. It should be feasible to optimize a single three node circuit using a normal computer, although considering the full set does require more computational resources.

A. All Two Node Circuits

We return to two node circuits and optimize their performance with the wider parameter ranges outlined in Sec. VI B. There are four total circuits to consider. As

Base Graph	Circuit	N_{gate} (Mean)	N_{gate} (Std)
1	J	$3.8 \cdot 10^3$	$1.8 \cdot 10^2$
	JL	$9.0 \cdot 10^4$	$1.4 \cdot 10^3$
	CJ	$4.1 \cdot 10^4$	$8.6 \cdot 10^2$
	CJL	$1.9 \cdot 10^5$	$6.0 \cdot 10^3$

TABLE VII. Optimized number of gates for all two node circuits. this maximum value of $N_{\text{gate}} = 187,000 \approx 1.9 \times 10^5$ for an optimized fluxonium will serve as a benchmark for larger circuits.

seen in table VII, the capacitively shunted fluxonium circuit CJL scored the highest of all two node circuits, with an average $N_{\text{gate}} = 187,000$. This value was achieved with $E_C = 2.63$ GHz, $E_J = 2.85$ GHz, $E_L = 0.51$ GHz, and $\varphi_{\text{ext}} = 0$. The system appears to be a lower frequency version of the optimized fluxonium from Fig. 10, with a reduced dependence on external flux due to the larger inductor.

As we turn our attention to three node circuits, this maximum value of $N_{\text{gate}} = 187,000 \approx 1.9 \times 10^5$ for an optimized fluxonium will serve as a benchmark.

B. All Three Node Circuits

For three node circuits there are 88 circuits, which is too many to list explicitly. Instead, we show the top few performers, split on different secondary characteristics such as base graph, number of junctions, number of flux loops, and number of charge modes. To read the tables below keep in mind that if the circuit is described with one comma, e.g. “JC, JL” it means it is a linear base graph whereas two commas indicates a delta base graph e.g. “JC, JL, J”.

Base Graph	Circuit	N_{gate} (Mean)	N_{gate} (Std)
1	JL, CJL	$1.9 \cdot 10^5$	$5.6 \cdot 10^3$
	CJL, CJL	$1.9 \cdot 10^5$	$5.0 \cdot 10^3$
	CL, CJ	$1.2 \cdot 10^5$	$2.3 \cdot 10^3$
	J, CJL	$9.5 \cdot 10^4$	$1.2 \cdot 10^3$
2	J, L, CL	$2.8 \cdot 10^5$	$1.6 \cdot 10^4$
	J, CL, CL	$2.5 \cdot 10^5$	$1.1 \cdot 10^4$
	J, L, JL	$2.4 \cdot 10^5$	$1.8 \cdot 10^4$
	CL, CL, CJ	$2.4 \cdot 10^5$	$1.1 \cdot 10^4$

TABLE VIII. Optimized number of gates for all three node circuits, split by base graph, see Fig. 3. The Δ topology (base graph 2) outperforms the linear graph (base graph 1).

In table VIII we split results by base graph. Circuits with the linear base graph 1 have comparable performance to the 2 node circuits, with a slightly smaller standard deviation. Base graph 2, the delta topology, sees an improvement between $1.2 \lesssim N_{\text{gate}} \lesssim 1.5$ relative to the $N_{\text{gate}} \approx 1.9 \times 10^5$ for the two node circuits, at the cost of sensitivity to fabrication variation).

N_{JJ}	Circuit	N_{gate} (Mean)	N_{gate} (Std)
1	J, L, CL	$2.8 \cdot 10^5$	$1.6 \cdot 10^4$
	J, CL, CL	$2.5 \cdot 10^5$	$1.1 \cdot 10^4$
	CL, CL, CJ	$2.4 \cdot 10^5$	$1.1 \cdot 10^4$
2	J, L, JL	$2.4 \cdot 10^5$	$1.8 \cdot 10^4$
	L, JL, CJ	$2.4 \cdot 10^5$	$1.1 \cdot 10^4$
	C, CJL, CJL	$1.9 \cdot 10^5$	$5.5 \cdot 10^3$
3	CJ, CJL, CJL	$1.9 \cdot 10^5$	$3.1 \cdot 10^3$
	JL, JL, CJ	$1.3 \cdot 10^5$	$2.0 \cdot 10^4$
	JL, CJ, CJL	$1.2 \cdot 10^5$	$3.4 \cdot 10^3$

TABLE IX. Optimized number of gates for all three node circuits, split by number of junctions N_{JJ} . Circuits with fewer junctions perform better than those with more junctions.

In tables IX to XI we split by JJs, number of charge modes, number of flux loops respectively. Broadly speaking, these splits tell us about the relative importance of charge and flux noise when modeling the number of gates. From table IX, we infer that fewer JJs are preferred by our model. From table X, we infer that 1 or 2 flux loops is preferred over 0, 3, or 4 loops. These preferences may be a reflection of the limited design space of three node circuits. More flux loops means a higher sensitivity to flux noise, and with only three nodes, it is difficult to add more junctions without creating new flux loops. In table XI, we additionally see that periodic modes are heavily penalized. Again this may be because of the limited configurations available in three node circuits.

Finally we look at two of our top performing circuits in more detail. We choose circuits “J, L, CL” and “J, L, JL” because they are highest performing circuits with

N_{loop}	Circuit	N_{gate} (Mean)	N_{gate} (Std)
0	C, J, CL	$1.2 \cdot 10^5$	$4.8 \cdot 10^3$
	C, J, L	$1.2 \cdot 10^5$	$5.6 \cdot 10^3$
1	J, L, CL	$2.8 \cdot 10^5$	$1.6 \cdot 10^4$
	J, CL, CL	$2.5 \cdot 10^5$	$1.1 \cdot 10^4$
2	J, L, JL	$2.4 \cdot 10^5$	$1.8 \cdot 10^4$
	L, JL, CJ	$2.4 \cdot 10^5$	$1.1 \cdot 10^4$
3	CJ, CJL, CJL	$1.9 \cdot 10^5$	$3.1 \cdot 10^3$
	JL, JL, CJ	$1.3 \cdot 10^5$	$2.0 \cdot 10^4$
4	CJL, CJL, CJL	$7.0 \cdot 10^4$	$10.0 \cdot 10^2$
	JL, JL, CJL	$6.6 \cdot 10^4$	$6.7 \cdot 10^2$

TABLE X. Optimized number of gates for all three node circuits, split by number of flux loops N_{loop} . Circuits with one or two loops score the highest.

N_{periodic}	Circuit	N_{gate} (Mean)	N_{gate} (Std)
0	J, L, CL	$2.8 \cdot 10^5$	$1.6 \cdot 10^4$
	J, CL, CL	$2.5 \cdot 10^5$	$1.1 \cdot 10^4$
	J, L, JL	$2.4 \cdot 10^5$	$1.8 \cdot 10^4$
1	C, J, CJL	$1.9 \cdot 10^5$	$4.6 \cdot 10^3$
	C, CJ, CJL	$1.9 \cdot 10^5$	$3.8 \cdot 10^3$
	C, JL, CJ	$1.9 \cdot 10^5$	$5.1 \cdot 10^3$
2	J, J, J	$6.7 \cdot 10^4$	$1.9 \cdot 10^3$
	J, J, CJ	$6.0 \cdot 10^4$	$1.7 \cdot 10^3$
	CJ, CJ	$4.5 \cdot 10^4$	$6.2 \cdot 10^2$

TABLE XI. Optimized number of gates for all three node circuits, split by number of periodic modes N_{periodic} . Circuits with fewer periodic modes perform better.

one and two Josephson junctions respectively. The highest performer “J, L, CL” belongs to Hamiltonian class 3 – 7, which consists of coupled extended and harmonic modes. As seen in Fig. 11 (a-c), the wavefunctions of the optimized circuit appear fluxonium-like and harmonic oscillator-like in the respective directions. The charge dispersion appears fluxonium like, with some reduction in sensitivity. The circuit “J, L, JL” belongs to the more interesting Hamiltonian class 3 – 19, which is composed of two nonlinearly coupled extended modes. As seen in Fig. 11 (d-f), the first three energy levels are highly non-localized across nine potential wells. The system is insensitive to flux through the junction/inductor loop, but it has some sensitivity to the main loop. This system is less easily mapped onto familiar single mode circuits, although to an extent it most closely resembles a 2D version of the Bloch qubit [90, 91].

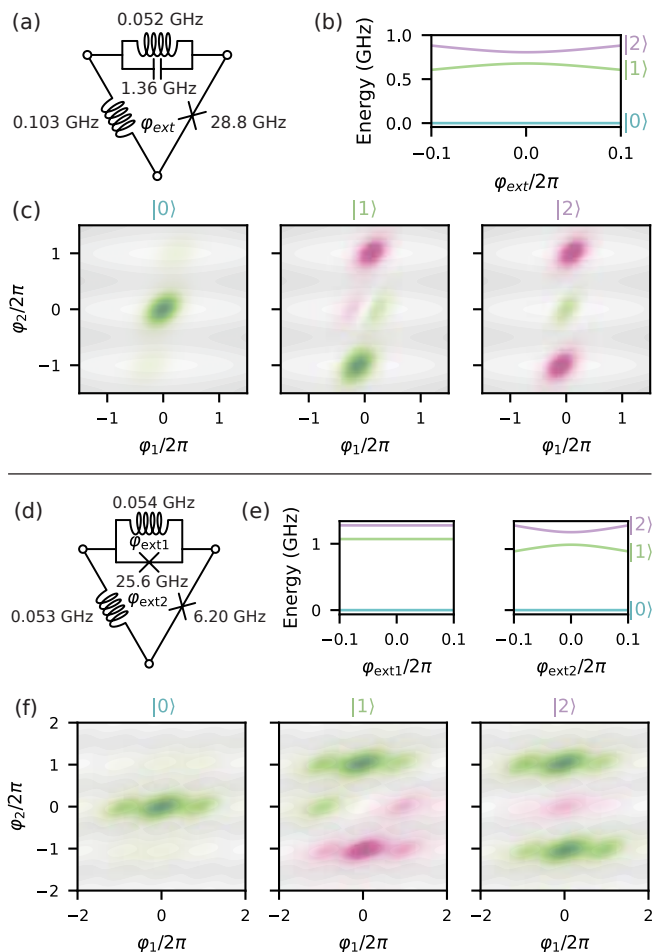


FIG. 11. The top performing circuits “J, L, CL” (a-c) and “J, L, JL” (d-f). The two circuits are in Hamiltonian classes 3 – 7 and 3 – 19 respectively. (a & d) show the circuit diagrams, annotated with parameter values. All junctions are given an additional capacitance $E_{C_J} = 10$ GHz. (b & e) show the flux dispersion around the optimized operating point. (c & f) provide the wavefunctions of the lowest three energy eigenstates, normalized to the phase of the peak of the $|0\rangle$ state. Here green is positive and pink is negative. The grey background is a contour of the potential energy landscape, with white being low energy and dark grey being high energy. The wavefunctions of the optimized “J, L, CL” appear fluxonium-like and harmonic oscillator-like in the respective directions, while they are highly non-localized across nine potential wells for “J, L, JL.”

VIII. CONCLUSION

We have enumerated all nonlinear superconducting circuits up-to five nodes in size consisting of capacitors, inductors, and Josephson junctions. These circuits could be used as amplifiers, current mirrors, or qubits. In classical electronics, large nonlinear circuits are constructed from well-understood smaller modules. For nonlinear superconducting circuits, we have arguably enumerated most smaller modules that a human can understand.

Another interesting perspective comes from Mendeleev-like tables in superconducting qubits [92]. Recall that the Mendeleev table, or periodic table, organizes elements by their atomic numbers, revealing trends, where elements in the same group exhibit similar chemical behaviours. In superconducting qubits we represent the family of CJL circuits as points in the 2D space or “table” of E_L/E_C and E_J/E_C [93, 94]. In this sense, each marked point in our parameter sweep from Fig. 9 (b) would represent a different qubit on the Mendeleev-like table. These plots provide a simple framework to understand the differences between most superconducting qubits built today [92]. The key intuition is that varying circuit parameters unlocks distinct behaviors, and the analogy works well for single-mode circuits. Our results suggest a different categorization for multimode circuits. Harmonic, periodic, and extended modes can be seen as “atoms,” with different circuits as “molecules” made of these atoms. Varying parameters like E_J or E_L could produce different “species” or isotopes of the underlying atoms. In the expanded analogy, the atoms (modes), bonds (inter-mode coupling), and atomic species (circuit parameters) all combine to dictate the behavior of a superconducting circuit “molecule.” Our work has thus begun building a catalog of possible molecules for use in building larger superconducting circuits.

The ultimate goal of this enumeration study is to catalog the space of possible circuits. The insights gained from this work can then enhance circuit design and synthesis tasks. We constructed a minimal set of unique circuits, eliminating over 100,000 equivalent diagrams in the case of four node circuits (and over 300,000,000 for five node circuits). We began classifying the circuits based on the type and quantity of operators present in their quantum Hamiltonians. In the case of four and five node circuits, we saw a reduction from 139,944 and 338,332,113 circuits to only 165 and 3546 Hamiltonian classes respectively. By optimizing over unique circuits or Hamiltonian classes, one can focus on unique configurations and efficiently and thoroughly search the design space.

As a proof of concept, we optimized over all three node circuits for qubit performance. Our numerics indicated that the best three node circuit might have a small but significant improvement in the number of gates that can be performed in a coherence time relative to the best fluxonium circuits

$$N_{\text{gates}}^{\text{new circuit}} \approx 1.5 \times N_{\text{gates}}^{\text{Fluxonium}}.$$

As three node circuits only have at most two modes, the kinds of Hamiltonians are limited and so is the improvement in number of gates. Our procedure also makes the key assumption that the qubit states are the ground and first excited states. With more flexibility in the qubit definition and more sophisticated gate time estimates, it may be possible to identify better configurations. A different loss function that aims for a desired property e.g. a particular level structure could also be used.

It is likely that four node circuits, which can have richer mode structure and couplings, will have higher performance, albeit at the cost of control and fabrication complexity. To perform a similar optimization over four node circuits would require more efficient modeling and optimization algorithms. A recent version of `SQcircuit` has added automatic differentiation to their superconducting circuit modeling, allowing for gradient aware optimization methods [63]. We are aware of at least two additional efforts towards auto-differentiation or GPU support in modeling superconducting qubits [95, 96]. More efficient methods such as tensor networks have also been suggested [97]. These computational advances will be crucial when studying more complicated circuits.

There are many paths to follow in future work. It is straightforward to extend our procedure to other two terminal devices. For example, we have enumerated all four node circuits including a quantum phase slip junction (QPS) `Q` constructed from the components

$$C, J, L, Q, CJ, CL, CQ, JL, \text{ and } JQ.$$

At present, systematic circuit quantization with QPS is still an active area of research, so we cannot proceed with the circuit analysis [69, 74]. Extending our enumeration to multiterminal devices, such as gyrators, will be much more difficult due to the hardness of the graph theory.

In our opinion, the most productive area for future work would be developing the concept of Hamiltonian classes, perhaps through the theory of equivalent Hamiltonians or Lagrangians. By putting Hamiltonian enumeration on a rigorous theoretical footing, the space of superconducting circuits could be more meaningfully catalogued, providing an advanced starting point for any circuit synthesis task. Such an analysis could also – from the Hamiltonians themselves – shed light on the fundamental capabilities and limitations of nonlinear superconducting circuits.

Acknowledgements: The authors thank Joe Aumentado, Juan Camilo, Sai Pavan Chitta, Xanthe Croot, Robert W. Erickson, Peter Groszkowski, Jens Koch, Florent Lecocq, Zachary Parrott, Taha Rajabzadeh, Javad Shabani, and Thomas Smith for helpful discussions. EW was supported by the National Science Foundation Graduate Research Fellowship under Grant No. 2040434. MB was supported through CU Boulder’s Discovery Learning Apprenticeship (DLA) program. JC and ZL were supported by the National Science Foundation through a CAREER award ECCS-2240129.

Appendix A: Subtleties in the Enumeration

Enumerating all possible circuits is a formidable endeavor. Although we have completed this enumeration, this is under some assumptions. In this appendix, we delve into further intricacies that we did not consider our study, with a focus on how these factors impact the systems derived from our enumerated circuits. For example

our enumeration did not explore practical things like: stray capacitances or inductances, readout resonators, transmission lines, and Purcell filters. We fully acknowledge that this overview is not exhaustive, nor is it possible to consider all such intricacies in a single study.

1. Ground Placement and Circuit Equivalence

Our enumeration procedure does not assign any nodes to ground, although the placement of the ground node can significantly change the system’s Hamiltonian. We are forced to make this choice when modeling our circuits in Sec. VII.

As it pertains to circuit enumeration, a choice of multiple ground nodes can also change the effective circuit topology. Consider the two circuits in Fig. 12 (a) and (b) which have four and 3 nodes respectively. If we ground two nodes in Fig. 12 (a) and one node in Fig. 12 (b) we arrive at a circuit that looks like galvanically coupled transmons. As a result, our procedure can overcount the number of unique circuits when grounds are included. For each graph of N nodes there are $\sum_{k=1}^{N-1} \binom{N}{k} = 2^N - 2$ ways of grounding a circuit. Enumerating these possibilities and identifying equivalent configurations would be possible by including an extra ground “color” into the graph isomorphism procedure described in Sec. III. However, it should be noted that grounding multiple nodes effectively reduces the number of nodes in a circuit. So, these smaller circuits do not represent new configurations and will show up in the enumeration of smaller circuits.

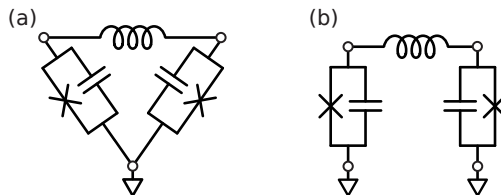


FIG. 12. An illustration of how the placement and number of grounds in a circuit can induce isomorphism. Circuit (a) has three nodes while circuit (b) has four nodes. The circuits are made equivalent by grounding the specified one (a) and two (b) nodes shown.

2. Ambiguities related to SQUIDs and linearization

We did not include superconducting quantum interference devices (SQUIDs) or tunable inductors constructed from flux biased SQUIDs in our enumeration. In some sense, every JJ could be considered as a split junction ie. SQUID. Also every linear inductor could be understood as a linearized SQUIDs, see Fig. 13. These differences make a big difference when considering the Hamiltonian,

as there is an extra tunable degree of freedom $(\phi - \phi_{\text{ext}})^2$ and $\cos(\phi - \phi_{\text{ext}})$.

It should also be noted that by manipulating these biases, it is possible to construct schemes that produce effective cubic or quartic terms [98, 99]. The classic example is of the SNAIL [98]. The circuit for the snail consists of several JJs in a series/parallel combination, wherein by tuning the external flux through the circuit, it is possible to effectively isolate certain powers of the phase operator ϕ^n . To include such effects, we could imagine adding several new dipole elements. This is an interesting possibility that could yield interesting systems, but such cases are not accounted for by our enumeration procedure.

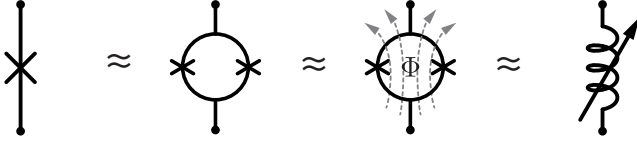


FIG. 13. Flux tunable elements not explicitly considered by our enumeration procedure include SQUIDS (tunable junction) and linearized SQUIDS (tunable inductor).

3. Charge and Flux bias

We do not consider charge and flux biases, see e.g. Fig. 14, directly in our enumeration, although they do appear in the optimization over unique circuits. The presence of these bias terms would differentiate different circuits in the same Hamiltonian class (described in Sec. IV).

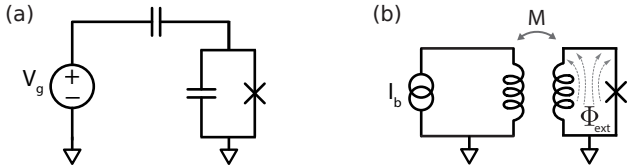


FIG. 14. Example (a) charge bias circuit and (b) flux bias, neither of which are not explicitly considered by the enumeration procedure.

To see this is the case, consider the circuit Hamiltonian

$$H = \frac{1}{2}(Q - C_V V)^T C^{-1}(Q - C_V V) + U(\Phi, \Phi_{\text{ext}}), \quad (\text{A1})$$

where Q is the vector of node charge variables, Φ is the vector of node flux variables, C^{-1} is the inverse capacitance matrix, and V & C_V are classical voltage variables and capacitive connections to them respectively. We can separate this as an effective circuit and coupling Hamil-

tonian:

$$H_{\text{circuit}} = \frac{1}{2}Q^T C^{-1}Q + U(\Phi) \quad (\text{A2})$$

$$H_{\text{coupling}} = Q^T C^{-1}C_V V + U(\Phi, \Phi_{\text{ext}}). \quad (\text{A3})$$

We focus exclusively on H_{circuit} when considering the enumerated Hamiltonians in Sec. IV. This is equivalent to considering the full Hamiltonian with $V = \Phi_{\text{ext}} = 0$. Different circuits with identical H_{circuit} (i.e., in the same class) may have a variety in H_{coupling} . This difference provides different degrees of freedom with which to control the system (and which may impact decoherence properties differently). The effects of different charge and flux biases should be considered for future attempts to analyze these sets of Hamiltonians.

4. Circuit Elements Not Considered

There are several elements that we did not include in our main enumeration that appear to some extent in the superconducting circuit literature. For example resistors and three terminal devices e.g. a circulators. It is worthwhile to comment on two specific cases in a little more detail. See Fig. 15.

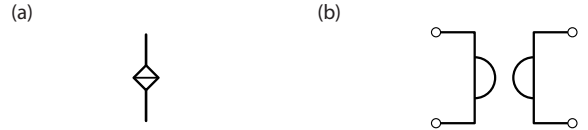


FIG. 15. QPS and multi terminal or port devices

Quantum Phase Slip junction or QPS [100], is effectively a nonlinear capacitor that is the electrical dual to the JJ. Although this component has yet to see an unequivocal experimental realization, we chose to exclude it from the main work, as it has not yet been included in modern superconducting qubit analysis packages. This would practically limit the analysis of the circuits produced. However it is straightforward to add any additional two terminal device for only the circuit enumeration and reduction steps. Indeed to begin exploring circuits containing QPS, we performed a secondary enumeration considering circuits up to four nodes in size with the elements

C, J, L, Q, CL, JL, CQ, and JQ.

Non-reciprocal devices such as circulators or gyrators are multiport/terminal non-reciprocal devices. There seems to be two issues (i) issues related to non-reciprocity, (ii) issues related to the multiport nature of the device. The non-reciprocity issue is that we have only recently seen consistent quantization of non-reciprocal devices [74], so again software packages do not support this. The multiport issue would add significant overhead to the enumeration procedure. In short,

circuit topologies would have to be represented as directed hypergraphs instead of undirected graphs. In addition to increasing the number of possible configurations, this would limit our ability to leverage existing pre-compiled results, as non-isomorphic sets of simple graphs are widely available, while non-isomorphic sets of hypergraphs are not.

Appendix B: Gate Time Estimates

We estimate gate time by modeling an arbitrary superconducting qubit as a three-level atom. We consider driving either a direct transition, $|0\rangle \leftrightarrow |1\rangle$, or an indirect transition via the higher lying $|2\rangle$ state (Λ -type configuration), see Fig. 16. In practice, driving either of these in larger circuits may require difficult multi-node couplings. The key of this appendix is to include a simple treatment of leakage that is consistent between the direct and Raman style transitions. We compare the time required to transfer population from $|0\rangle \leftrightarrow |1\rangle$ using both schemes, subject to this leakage and other drive constraints, and use the faster of the two as our gate time estimate.

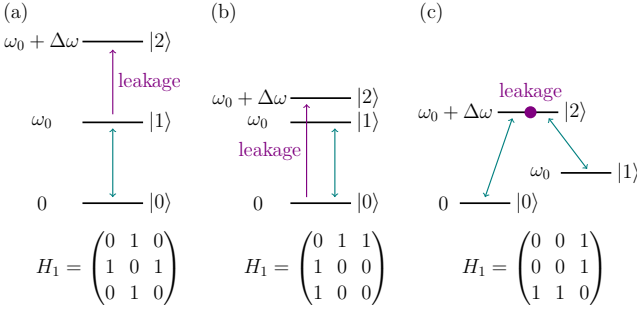


FIG. 16. The three types of transitions + leakages considered. (a) A weakly anharmonic qubit with a direct transition $|0\rangle \rightarrow |1\rangle$. Here the leakage is via the $|1\rangle \rightarrow |2\rangle$ transition. (b) A nearly degenerate second excited state qubit with a direct transition $|0\rangle \rightarrow |1\rangle$. In this case the leakage is via the $|0\rangle \rightarrow |2\rangle$ transition. (c) Raman type transition $|0\rangle \rightarrow |2\rangle \rightarrow |1\rangle$, with population remaining in $|2\rangle$ considered as leakage.

1. Direct Transition

We assume our qutrit Hamiltonian is of the form:

$$H = H_0 + f(t)H_1, \quad (\text{B1})$$

with the free Hamiltonian

$$H_0 = \begin{pmatrix} 0 & 0 & 0 \\ 0 & \omega_0 & 0 \\ 0 & 0 & \omega_0 + \Delta\omega \end{pmatrix}, \quad (\text{B2})$$

where $0 < |\Delta| \leq \omega_0$ and we have set the ground state energy to zero. In Fig. 16 we give the different cases we

consider, and in (a) the drive Hamiltonian is

$$H_1 = \begin{pmatrix} 0 & 1 & 0 \\ 1 & 0 & 1 \\ 0 & 1 & 0 \end{pmatrix}. \quad (\text{B3})$$

The upper right block is the qubit σ_X and the remainder is a leakage pathway. The particulars of the leakage pathway depends on which transition ($|0\rangle \leftrightarrow |2\rangle$ or $|1\rangle \leftrightarrow |2\rangle$) is closer in frequency to the $|0\rangle \leftrightarrow |1\rangle$ transition.

The drive $f(t)$ is taken to be a monotone drive ω_0 with a Gaussian pulse envelope $f(t) = V_0 e^{-t^2/2\tau} \cos(\omega_0 t)$. Here V_0 is the maximum drive amplitude. Generally, the magnitude of the matrix elements of H_1 (taken to be 1) depends on the coupling schemes used for a given circuit.

We expect population to transfer between $|0\rangle$ and $|1\rangle$ when the area under the envelope is equal to π (i.e., a π pulse). This corresponds to a pulse half-width of $\tau = \sqrt{\pi/2}/V_0$. By setting a maximum value for V_0 , we obtain a minimum gate time. However, fast gates have implications for leakage as well. The more compact a pulse is in time, the more broadband it is in frequency. This spectral broadening is the main source of leakage into the $|2\rangle$ state for transmon like systems, the DRAG protocol can combat this issue [101, 102].

To estimate this leakage, we consider the evolution of a two-tone Hamiltonian:

$$H_{2\text{-tone}} = \begin{pmatrix} 0 & 1 & 0 \\ 1 & 0 & \lambda \\ 0 & \lambda & 0 \end{pmatrix} \quad \text{or} \quad \begin{pmatrix} 0 & 1 & \lambda \\ 1 & 0 & 0 \\ \lambda & 0 & 0 \end{pmatrix}, \quad (\text{B4})$$

with $\lambda = |F(\omega_0 + \Delta\omega)/F(\omega_0)|$ or $\lambda = |F(\Delta\omega)/F(\omega_0)|$, the amplitude ratio of the fourier transform of the drive at the leakage transition compared with the qubit transition. In chapter 9.5 of Ref. [103], it is shown that for our choice of $f(t)$, we have

$$F(w) = \sqrt{\frac{\pi}{2}} \tau V_0 (e^{-(w-\omega_0)^2 \tau^2/2} + e^{-(w+\omega_0)^2 \tau^2/2}). \quad (\text{B5})$$

The amplitude ratio is thus $\lambda = e^{-\delta^2 \tau^2/2}$, with δ being the detuning between the leakage transition and the qubit transition (either $\Delta\omega - \omega_0$ or $\Delta\omega$ depending on the structure of the system).

Solving the time-independent Schrodinger equation for $|\psi(t=0)\rangle = |0\rangle$, the maximum probability to be in the $|1\rangle$ state (in both cases) is

$$P_{\text{max},|1\rangle} = \frac{1}{1 + \lambda^2} = \frac{1}{1 + e^{-\delta^2 \tau^2}}. \quad (\text{B6})$$

To obtain a gate time estimate, we substitute in $\tau = \sqrt{\pi/2}/V_0$ corresponding to a π pulse and solve for the V_0 required to achieve a population transfer of 99.9%

$$\frac{1}{1 + e^{-\delta^2 (\sqrt{\pi/2}/V_0)^2}} = 0.999 \rightarrow V_0 \approx \frac{\delta}{2}. \quad (\text{B7})$$

Finally, we set two maximum drive constraints. First, we work backwards from an absolute speed limit of $\tau_{\min} \approx 1$ ns for a π pulse to arrive at a maximum $V_{\max} = 200$ MHz. Second, we require that $10V_0 \leq \omega_0$ for direct transitions to remain in the regime of the physics described in this section. This leaves τ for a direct transition as

$$\tau_{g,\text{direct}} = \begin{cases} \sqrt{2\pi}/\delta, & \delta/2 \leq V_{\text{lim}} \\ \sqrt{\pi/2}/V_{\max}, & \delta/2 > V_{\text{lim}} \end{cases}, \quad (\text{B8})$$

with δ again being the detuning between ω_0 and the leakage transition ($|0\rangle \leftrightarrow |2\rangle$ or $|1\rangle \leftrightarrow |2\rangle$) and $V_{\text{lim}} = \min(V_{\max}, \omega_0/10)$. Note that reported gate times are set to 5τ , which corresponds to a pulse area of $\approx 99\%$ of the Gaussian envelope. We see three distinct limiting factors emerge from Eq. (B8): (1) τ increases when δ is small, (2) τ increases when ω_0 is small, and (3) the absolute speed limit (i.e., τ_{\min} is set by V_{\max}). In the case of Transmon like systems, factor (1) reproduces the conventional wisdom that gate time is inversely proportional to anharmonicity.

2. Raman-Type Gate

For transitions via $|2\rangle$, we take H_0 to be identical to the direct transition case, but we now consider

$$H_1 = \begin{pmatrix} 0 & 0 & 1 \\ 0 & 0 & 1 \\ 1 & 1 & 0 \end{pmatrix} \quad (\text{B9})$$

and drive both the $|0\rangle \leftrightarrow |2\rangle$ and $|1\rangle \leftrightarrow |2\rangle$ transitions by setting

$$f(t) = e^{-t^2/2\tau} [V_1 \cos(\omega_0 t - \Delta) + V_2 \cos(\Delta \omega t - \Delta)]. \quad (\text{B10})$$

If the system begins in $|\psi(t=0)\rangle = |0\rangle$, it experiences Rabi oscillations between $|0\rangle$ and $|1\rangle$ with an effective Rabi frequency of $\Omega_R = V_1 V_2 / 2\Delta$ [56]. The intermediate state population experiences oscillations with a maximum value of

$$P_{\max,|2\rangle} = \frac{V_1^2}{\Delta^2 + V_1^2 + V_2^2}. \quad (\text{B11})$$

Taking this maximum intermediate state population as a proxy for leakage, we find the τ required to limit leakage to 0.1% (equivalent to the 99.9% population transfer considered in the direct case). Taking $V_1 = V_2 = V$ and $\Delta = 30V$ yields an effective Rabi frequency of $\Omega_R = V/60$, with corresponding $\tau = 60\sqrt{\pi/2}/V$ for a π pulse. We assume here that there exists a spectrally isolated higher level state, so our only constraint is that $V \leq V_{\max}$. This gives τ for a Raman style transition of

$$\tau_{g,\text{raman}} = 60\sqrt{\pi/2}/V_{\max} \quad (\text{B12})$$

Taking $V_{\max} = 200$ MHz as in the direct transition, we get $\tau_{g,\text{raman}} \approx 60$ ns. Again, the gate time is taken to be 5τ to capture most of the pulse area. While V_{\max} in the direct transition established a minimum gate time, the same constraint here establishes a maximum gate time of approximately 300 ns.

The Raman-type gate will be preferred over the direct transition only in the cases of nearly degenerate ground states and very small anharmonicity. Due to the slow nature of these estimates, we do not consider leakage due to spectral broadening for the Raman style transition.

Appendix C: Modeling Implementation Details

In considering large numbers of unstudied circuits, we are forced to make key assumptions in how the systems are modeled. Many of these assumptions are taken for granted in transmon-like systems, although they can have profound impacts on how larger multi-mode systems are treated. We make an attempt to list important assumptions in our modeling, although we do not claim that this list is exhaustive.

Selection of computational states. The computational states are taken to be the ground state and first excited states: $|0\rangle_L = |0\rangle$ and $|1\rangle_L = |1\rangle$. As outlined in appendix B, the dominant state for leakage errors is assumed to be the second excited state $|2\rangle$.

1/f Noise Amplitudes. We use the `SQcircuit` default values of 10^{-4} , 10^{-6} , and 10^{-7} for charge, flux, and critical current noise respectively. These values align with the lower bounds layed out in [78].

Hilbert Space Cutoff. `SQcircuit` models periodic modes in a charge basis and extended modes in a fock basis. To choose the number of states used in each mode, 200 circuits are randomly initialized within the parameter search space. For each circuit, the cutoffs on each mode are increased by a fixed increment until the fractional change in the first five eigenvalues are all under 10^{-6} . To trade off speed and modeling accuracy, the cutoffs for the given circuit are chosen to be the 90th percentile of sampled points. Each optimal point is then re-evaluated with a cutoff chosen for the specific choice of parameters. Only 2 out of 88 circuits saw meaningful changes in predicted performance N_{gate} upon re-evaluation.

Optimizing Offsets Due to the potentially high sensitivity of a circuit's performance to external inputs, flux and charge offsets are treated as integer variables. They are allowed to take on the special values of 0, 0.25, 0.5, and 0.75 [ϕ_0 for flux], shifted slightly by 10^{-4} for charge noise and 10^{-6} for flux noise. These shifts are to avoid numerical effects at exactly 0 or 0.5 and represent a worst case DC offset error equal to the $1/f$ noise amplitudes used for T_ϕ calculations.

Coupling. It is possible to couple to directly couple to the offset charges and fluxes of a multimode circuit. This freedom is assumed in order to optimize the circuit performance as a function off these offsets. Additionally,

coupling capacitance for charge offsets are ignored when constructing a system's Hamiltonian.

Parameter values. We limit the underlying circuit parameters to close to experimentally realized values. We consider Josephson junctions to have a fixed small capacitance. See Sec. [VIB](#) for more details.

Ground Placement. The choice of ground node in a circuit can have a significant effect on the circuit's performance. We consider weak capacitive coupling to ground from each node. Alternatively, grounding individual nodes of the circuit diagram could be considered, and the component graph isomorphism technique detailed in Sec. [IIIB](#) could be used to determine unique placements of the ground node. When grounding only a single node, circuits with dangling edges, or elements that cannot carry current, could be ignored.

Appendix D: Converting Between Physical and Frequency Units for Circuit Parameters

Consider dimensionfull (Φ, Q) and dimensionless (φ, q) flux and charge operators

$$q = \frac{Q}{2e}, \quad \& \quad \varphi = \frac{2\pi}{\Phi_0}\Phi. \quad (\text{D1})$$

Here e is the charge of a single electron, and Φ_0 is the magnetic flux quantum. E_C & E_L for a single element is related to physical capacitance C and inductance L by

$$hE_C = \frac{e^2}{2C}, \quad \& \quad hE_L = \frac{(\Phi_0/2\pi)^2}{L}. \quad (\text{D2})$$

These definitions ensure the energy stored in a capacitor with capacitance C and an inductor with inductance L

$$4E_C q^2 = \frac{1}{2C} Q^2, \quad \& \quad \frac{1}{2} E_L \varphi^2 = \frac{1}{2L} \Phi^2, \quad (\text{D3})$$

is consistent between dimensionless and dimension-full units.

Appendix E: Full Transmon/Fluxonium Parameter Sweeps

Fig. [17](#), details the decays and gate time estimates from Fig. [9](#) from the main text.

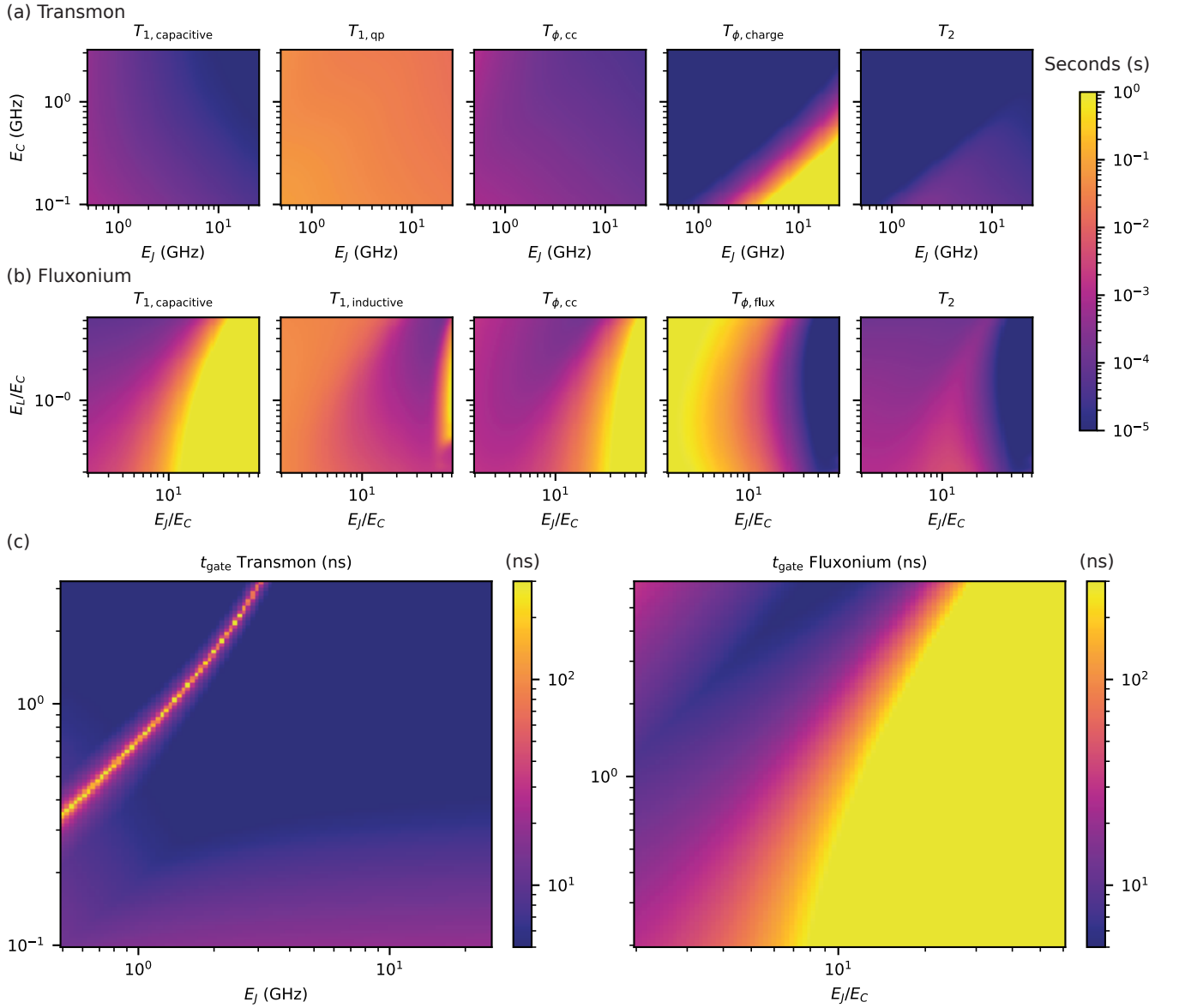


FIG. 17. Underlying coherence times and gate times estimates for the number of gates N_{gate} estimates in Fig. 9. Noise estimates from SQcircuit are shown for (a) transmon and (b) fluxonium. Channels not shown did not contribute meaningfully for the respective systems. Gate time estimates based on the analysis given in appendix B are shown in (c). The gate time estimates for the transmon seem consistent with gate times from the literature. It is important to note removing noises or reducing the noise magnitude will change the conclusion of our numerics.

-
- [1] J. A. Fleming, [Instrument for converting alternating electric currents into continuous currents](#) (1905).
 - [2] L. D. Forest, [Oscillation-responsive device](#) (1906).
 - [3] A. Sedra, K. Smith, T. C. Carusone, and V. Gaudet, *Microelectronic circuits 8th edition* (Oxford University Press, London, 2020).
 - [4] A. Blais, A. L. Grimsmo, S. M. Girvin, and A. Wallraff, Circuit quantum electrodynamics, *Rev. Mod. Phys.* **93**, 025005 (2021).
 - [5] D. R. Herber, T. Guo, and J. T. Allison, Enumeration of Architectures With Perfect Matchings, *Journal of Mechanical Design* **139**, 10.1115/1.4036132 (2017).
 - [6] D. R. Herber, *Advances in combined architecture, plant, and control design*, [Ph.D. thesis](#), University of Illinois at Urbana-Champaign (2017).
 - [7] P. Groszkowski and J. Koch, Scqubits: a Python pack-

- age for superconducting qubits, *Quantum* **5**, 583 (2021).
- [8] S. P. Chitta, T. Zhao, Z. Huang, I. Mondragon-Shem, and J. Koch, Computer-aided quantization and numerical analysis of superconducting circuits, *New Journal of Physics* **24**, 103020 (2022).
 - [9] D. Cucurachi, A. Guthrie, J. Heinsoo, S. Inel, D. Janzso, M. Jenei, K. Juliusson, J. Kotilahti, A. Landra, C. Ockeloen-Korppi, J. Rabinä, N. Savola, P. Smirnov, and E. Takala, *KQCircuits* (2021).
 - [10] M. F. Gely and G. A. Steele, Qucat: quantum circuit analyzer tool in python, *New Journal of Physics* **22**, 013025 (2020).
 - [11] P. Aumann, T. Menke, W. D. Oliver, and W. Lechner, Circuitq: an open-source toolbox for superconducting circuits, *New Journal of Physics* **24**, 093012 (2022).
 - [12] T. Rajabzadeh, Z. Wang, N. Lee, T. Makihara, Y. Guo, and A. H. Safavi-Naeini, Analysis of arbitrary superconducting quantum circuits accompanied by a Python package: SQcircuit, *Quantum* **7**, 1118 (2023).
 - [13] T. Tanamoto, T. Ishikawa, K. Inomata, S. Masuda, T. Omuma, and S. Kawabata, Classical spice simulation of superconducting quantum circuits, *Applied Physics Express* **16**, 034501 (2023).
 - [14] S. Darlington, A history of network synthesis and filter theory for circuits composed of resistors, inductors, and capacitors, *IEEE Transactions on Circuits and Systems* **31**, 3 (1984).
 - [15] G. A. Campbell and R. M. Foster, Maximum Output Networks for Telephone Substation and Repeater Circuits, *Transactions of the American Institute of Electrical Engineers* **XXXIX**, 231 (1920).
 - [16] P. A. MacMahon, Yoke-Chains and Multipartite Compositions in connexion with the Analytical forms called "Trees", *Proceedings of the London Mathematical Society* **s1-22**, 330 (1890).
 - [17] N. Howitt, Group Theory and the Electric Circuit, *Phys. Rev.* **37**, 1583 (1931).
 - [18] O. Brune, Equivalent Electrical Networks, *Phys. Rev.* **38**, 1783 (1931).
 - [19] O. Brune, Synthesis of a Finite Two-terminal Network whose driving-point impedance is a prescribed function of frequency, *Journal of Mathematics and Physics* **10**, 191 (1931).
 - [20] R. M. Foster, Geometrical Circuits of Electrical Networks, *Transactions of the American Institute of Electrical Engineers* **51**, 309 (1932).
 - [21] B. D. H. Tellegen, Geometrical configurations and duality of electrical networks, *Philips Technical Review* **5**, 324 (1940).
 - [22] J. Riordan and C. E. Shannon, The Number of Two-Terminal Series-Parallel Networks, *Journal of Mathematics and Physics* **21**, 83 (1942).
 - [23] L. Carlitz and J. Riordan, The number of labeled two-terminal series-parallel networks, *Duke Mathematical Journal* **23**, 435 (1956).
 - [24] V. Belevitch, Summary of the History of Circuit Theory, *Proceedings of the IRE* **50**, 848 (1962).
 - [25] P. Mateti and N. Deo, On Algorithms for Enumerating All Circuits of a Graph, *SIAM Journal on Computing* **5**, 90 (1976).
 - [26] H. Watanabe and S. Shinoda, Soul of circuit theory. A review on research activities of graphs and circuits in Japan, *IEEE Transactions on Circuits and Systems I: Fundamental Theory and Applications* **46**, 83 (1999).
 - [27] D. J. Lohan, Topology optimization methods for heat sink design applied to power electronics, *PhD thesis, University of Illinois at Urbana-Champaign* (2019).
 - [28] A. Morelli, Synthesis of electrical and mechanical networks of restricted complexity, *PhD thesis, University of Cambridge (Gonville & Caius College)* (2019).
 - [29] W. W. Happ, Combinatorial analysis of multi-terminal devices, *IEEE Transactions on Systems Science and Cybernetics* **3**, 21 (1967).
 - [30] A. S. Perelson, Description of electrical networks using bond graphs, *International Journal of Circuit Theory and Applications* **4**, 107 (1976).
 - [31] A. Reibiger, Networks, multipoles and multiports, in *2013 European Conference on Circuit Theory and Design (ECCTD)* (2013) pp. 1–37.
 - [32] F. Bruccoleri, E. Klumperink, and B. Nauta, Generating all two-mos-transistor amplifiers leads to new wide-band Inas, *IEEE Journal of Solid-State Circuits* **36**, 1032 (2001).
 - [33] E. Klumperink, F. Bruccoleri, and B. Nauta, Finding all elementary circuits exploiting transconductance, *IEEE Transactions on Circuits and Systems II: Analog and Digital Signal Processing* **48**, 1039 (2001).
 - [34] D. Shahhosseini, E. Zailer, L. Behjat, and L. Belostotski, Method of generating unique elementary circuit topologies méthode de génération de topologies de circuits élémentaires uniques, *Canadian Journal of Electrical and Computer Engineering* **41**, 118 (2018).
 - [35] H. Pretl and M. Eberlein, Fifty nifty variations of two-transistor circuits: A tribute to the versatility of mosfets, *IEEE Solid-State Circuits Magazine* **13**, 38 (2021).
 - [36] W. Lyu, P. Xue, F. Yang, C. Yan, Z. Hong, X. Zeng, and D. Zhou, An efficient bayesian optimization approach for automated optimization of analog circuits, *IEEE Transactions on Circuits and Systems I: Regular Papers* **65**, 1954 (2018).
 - [37] Z. Zhao and L. Zhang, Analog integrated circuit topology synthesis with deep reinforcement learning, *IEEE Transactions on Computer-Aided Design of Integrated Circuits and Systems* **41**, 5138 (2022).
 - [38] M. Fayazi, M. T. Taba, E. Afshari, and R. Dreslinski, Angel: Fully-automated analog circuit generator using a neural network assisted semi-supervised learning approach, *IEEE Transactions on Circuits and Systems I: Regular Papers* **70**, 4516 (2023).
 - [39] B. Yurke and J. S. Denker, Quantum network theory, *Phys. Rev. A* **29**, 1419 (1984).
 - [40] L. Chua and J. McPherson, Explicit topological formulation of Lagrangian and Hamiltonian equations for nonlinear networks, *IEEE Transactions on Circuits and Systems* **21**, 277 (1974).
 - [41] G. Bernstein and M. Lieberman, A method for obtaining a canonical Hamiltonian for nonlinear LC circuits, *IEEE Transactions on Circuits and Systems* **36**, 411 (1989).
 - [42] L. Weiss and W. Mathis, A Hamiltonian formulation for complete nonlinear RLC-networks, *IEEE Transactions on Circuits and Systems I: Fundamental Theory and Applications* **44**, 843 (1997).
 - [43] V. Bouchiat, D. Vion, P. Joyez, D. Esteve, and M. H. Devoret, Quantum Coherence with a Single Cooper Pair, *Physica Scripta* **T76**, 165 (1998).
 - [44] Y. Nakamura, Y. A. Pashkin, and J. S. Tsai, Coherent control of macroscopic quantum states in a single-cooper-pair box, *Nature* **398**, 786 (1999).

- [45] D. Vion, A. Aassime, A. Cottet, P. Joyez, H. Pothier, C. Urbina, D. Esteve, and M. H. Devoret, Manipulating the quantum state of an electrical circuit, *Science* **296**, 886 (2002).
- [46] J. M. Martinis, S. Nam, J. Aumentado, and C. Urbina, Rabi oscillations in a large josephson-junction qubit, *Phys. Rev. Lett.* **89**, 117901 (2002).
- [47] I. Chiorescu, Y. Nakamura, C. J. P. M. Harmans, and J. E. Mooij, Coherent quantum dynamics of a superconducting flux qubit, *Science* **299**, 1869 (2003).
- [48] A. Wallraff, D. I. Schuster, A. Blais, L. Frunzio, R. S. Huang, J. Majer, S. Kumar, S. M. Girvin, and R. J. Schoelkopf, Strong coupling of a single photon to a superconducting qubit using circuit quantum electrodynamics, *Nature* **431**, 162 (2004).
- [49] D. I. Schuster, A. A. Houck, J. A. Schreier, A. Wallraff, J. M. Gambetta, A. Blais, L. Frunzio, J. Majer, B. Johnson, M. H. Devoret, S. M. Girvin, and R. J. Schoelkopf, Resolving photon number states in a superconducting circuit, *Nature* **445**, 515 (2007).
- [50] S. Krinner, N. Lacroix, A. Remm, A. Di Paolo, E. Genois, C. Leroux, C. Hellings, S. Lazar, F. Swiadek, J. Herrmann, G. J. Norris, C. K. Andersen, M. Müller, A. Blais, C. Eichler, and A. Wallraff, Realizing repeated quantum error correction in a distance-three surface code, *Nature* **605**, 669 (2022).
- [51] R. Acharya, L. Aghababaie-Beni, I. Aleiner, T. I. Andersen, M. Ansmann, F. Arute, K. Arya, A. Asfaw, N. Astrakhantsev, J. Atalaya, R. Babbush, D. Bacon, B. Ballard, J. C. Bardin, J. Bausch, A. Bengtsson, A. Bilmes, S. Blackwell, S. Boixo, G. Bortoli, A. Bourassa, J. Bovaird, L. Brill, M. Broughton, D. A. Browne, B. Buchea, B. B. Buckley, D. A. Buell, T. Burger, B. Burkett, N. Bushnell, A. Cabrera, J. Campero, H.-S. Chang, Y. Chen, Z. Chen, B. Chiaro, D. Chik, C. Chou, J. Claes, A. Y. Cleland, J. Cogan, R. Collins, P. Conner, W. Courtney, A. L. Crook, B. Curtin, S. Das, A. Davies, L. D. Lorenzo, D. M. Debroy, S. Demura, M. Devoret, A. D. Paolo, P. Donohoe, I. Drozdov, A. Dunsworth, C. Earle, T. Edlich, A. Eickbusch, A. M. Elbag, M. Elzouka, C. Erickson, L. Faoro, E. Farhi, V. S. Ferreira, L. F. Burgos, E. Forati, A. G. Fowler, B. Foxen, S. Ganjam, G. Garcia, R. Gasca, E. Genois, W. Giang, C. Gidney, D. Gilboa, R. Gosula, A. G. Dau, D. Graumann, A. Greene, J. A. Gross, S. Habegger, J. Hall, M. C. Hamilton, M. Hansen, M. P. Harrigan, S. D. Harrington, F. J. H. Heras, S. Heslin, P. Heu, O. Higgott, G. Hill, J. Hilton, G. Holland, S. Hong, H.-Y. Huang, A. Huff, W. J. Huggins, L. B. Ioffe, S. V. Isakov, J. Iveland, E. Jeffrey, Z. Jiang, C. Jones, S. Jordan, C. Joshi, P. Juhas, D. Kafri, H. Kang, A. H. Karamlou, K. Kechedzhi, J. Kelly, T. Khairi, T. Khat-tar, M. Khezri, S. Kim, P. V. Klimov, A. R. Klots, B. Kobrin, P. Kohli, A. N. Korotkov, F. Kostritsa, R. Kothari, B. Kozlovskii, J. M. Kreikebaum, V. D. Kurilovich, N. Lacroix, D. Landhuis, T. Lange-Dei, B. W. Langley, P. Laptev, K.-M. Lau, L. L. Guevel, J. Ledford, K. Lee, Y. D. Lensky, S. Leon, B. J. Lester, W. Y. Li, Y. Li, A. T. Lill, W. Liu, W. P. Livingston, A. Locharla, E. Lucero, D. Lundahl, A. Lunt, S. Madhuk, F. D. Malone, A. Maloney, S. Mandra, L. S. Martin, S. Martin, O. Martin, C. Maxfield, J. R. McClean, M. McEwen, S. Meeks, A. Megrant, X. Mi, K. C. Miao, A. Mieszala, R. Molavi, S. Molina, S. Montazeri, A. Morvan, R. Movassagh, W. Mruczkiewicz, O. Naaman, M. Neeley, C. Neill, A. Nersisyan, H. Neven, M. Newman, J. H. Ng, A. Nguyen, M. Nguyen, C.-H. Ni, T. E. O'Brien, W. D. Oliver, A. Opremcak, K. Ottosson, A. Petukhov, A. Pizzuto, J. Platt, R. Potter, O. Pritchard, L. P. Pryadko, C. Quintana, G. Ramachandran, M. J. Reagor, D. M. Rhodes, G. Roberts, E. Rosenberg, E. Rosenfeld, P. Roushan, N. C. Rubin, N. Saei, D. Sank, K. Sankaragomathi, K. J. Satzinger, H. F. Schurkus, C. Schuster, A. W. Senior, M. J. Shearn, A. Shorter, N. Shutty, V. Shvarts, S. Singh, V. Sivak, J. Skruzny, S. Small, V. Smelyanskiy, W. C. Smith, R. D. Somma, S. Springer, G. Sterling, D. Strain, J. Suchard, A. Szasz, A. Szein, D. Thor, A. Torres, M. M. Torunbalci, A. Vaishnav, J. Vargas, S. Vdovichev, G. Vidal, B. Villalonga, C. V. Heidweiller, S. Waltman, S. X. Wang, B. Ware, K. Weber, T. White, K. Wong, B. W. K. Woo, C. Xing, Z. J. Yao, P. Yeh, B. Ying, J. Yoo, N. Yosri, G. Young, A. Zalcman, Y. Zhang, N. Zhu, and N. Zobrist, *Quantum error correction below the surface code threshold* (2024), arXiv:2408.13687 version: 1.
- [52] J. Koch, T. M. Yu, J. Gambetta, A. A. Houck, D. I. Schuster, J. Majer, A. Blais, M. H. Devoret, S. M. Girvin, and R. J. Schoelkopf, Charge-insensitive qubit design derived from the Cooper pair box, *Physical Review A* **76**, 042319 (2007).
- [53] M. Tuokkola, Y. Sunada, H. Kivijärvi, J. Albanese, L. Grönberg, J.-P. Kaikkonen, V. Vesterinen, J. Govenius, and M. Möttönen, *Methods to achieve near-millisecond energy relaxation and dephasing times for a superconducting transmon qubit* (2024), arXiv:2407.18778.
- [54] V. E. Manucharyan, J. Koch, L. I. Glazman, and M. H. Devoret, Fluxonium: Single cooper-pair circuit free of charge offsets, *Science* **326**, 113 (2009).
- [55] A. Somoroff, Q. Ficheux, R. A. Mencia, H. Xiong, R. Kuzmin, and V. E. Manucharyan, Millisecond Coherence in a Superconducting Qubit, *Physical Review Letters* **130**, 267001 (2023).
- [56] A. Gyenis, A. Di Paolo, J. Koch, A. Blais, A. A. Houck, and D. I. Schuster, Moving beyond the Transmon: Noise-Protected Superconducting Quantum Circuits, *PRX Quantum* **2**, 030101 (2021).
- [57] A. Gyenis, P. S. Mundada, A. Di Paolo, T. M. Hazard, X. You, D. I. Schuster, J. Koch, A. Blais, and A. A. Houck, Experimental realization of a protected superconducting circuit derived from the $0-\pi$ qubit, *PRX Quantum* **2**, 010339 (2021).
- [58] F. Yan, Y. Sung, P. Krantz, A. Kamal, D. K. Kim, J. L. Yoder, T. P. Orlando, S. Gustavsson, and W. D. Oliver, *Engineering Framework for Optimizing Superconducting Qubit Designs* (2020), arXiv:2006.04130 [quant-ph].
- [59] F.-M. Liu, C. Wang, M.-C. Chen, H. Chen, S.-W. Li, Z.-X. Shang, C. Ying, J.-W. Wang, Y.-H. Huo, C.-Z. Peng, X. Zhu, C.-Y. Lu, and J.-W. Pan, Quantum computer-aided design for advanced superconducting qubit: Plasmonium, *Science Bulletin* **68**, 1625 (2023).
- [60] T. Menke, F. Häse, S. Gustavsson, A. J. Kerman, W. D. Oliver, and A. Aspuru-Guzik, Automated design of superconducting circuits and its application to 4-local couplers, *npj Quantum Information* **7**, 1 (2021), number: 1 Publisher: Nature Publishing Group.
- [61] F. A. Cárdenas-López, J. C. Retamal, X. Chen,

- G. Romero, and M. Sanz, [Resilient superconducting-element design with genetic algorithms](#) (2023), arXiv:2302.01837 [quant-ph].
- [62] P. García-Azorín, F. A. Cárdenas-López, G. B. P. Huber, G. Romero, M. Werninghaus, F. Motzoi, S. Filipp, and M. Sanz, [Robust multi-mode superconducting qubit designed with evolutionary algorithms](#) (2024), arXiv:2407.18895 [quant-ph].
- [63] T. Rajabzadeh, A. Boulton-McKeehan, S. Bonkowsky, D. I. Schuster, and A. H. Safavi-Naeini, [A General Framework for Gradient-Based Optimization of Superconducting Quantum Circuits using Qubit Discovery as a Case Study](#) (2024), arXiv:2408.12704.
- [64] S. Kumar, S. Tuli, J. Koch, N. Jha, and A. A. Houck, APS March Meeting 2024 – abstract: M48.00002 GraphQ: High-Coherence Superconducting Circuit Optimization using Graph Machine Learning, in *Bulletin of the American Physical Society* (American Physical Society, 2024).
- [65] B. McKay, [Combinatorial Data – Graphs – Simple graphs](#) (2023), <https://users.cecs.anu.edu.au/~bdm/data/graphs.html>.
- [66] N. Ofek, A. Petrenko, R. Heeres, P. Reinhold, Z. Leghtas, B. Vlastakis, Y. Liu, L. Frunzio, S. M. Girvin, L. Jiang, M. Mirrahimi, M. H. Devoret, and R. J. Schoelkopf, Extending the lifetime of a quantum bit with error correction in superconducting circuits, *Nature* **536**, 441 (2016).
- [67] Z. Ni, S. Li, X. Deng, Y. Cai, L. Zhang, W. Wang, Z.-B. Yang, H. Yu, F. Yan, S. Liu, C.-L. Zou, L. Sun, S.-B. Zheng, Y. Xu, and D. Yu, Beating the break-even point with a discrete-variable-encoded logical qubit, *Nature* **616**, 56 (2023).
- [68] V. V. Sivak, A. Eickbusch, B. Royer, S. Singh, I. Tsioutsios, S. Ganjam, A. Miano, B. L. Brock, A. Z. Ding, L. Frunzio, S. M. Girvin, R. J. Schoelkopf, and M. H. Devoret, Real-time quantum error correction beyond break-even, *Nature* **616**, 50 (2023).
- [69] A. Osborne, T. Larson, S. G. Jones, R. W. Simmonds, A. Gyenis, and A. Lucas, Symplectic geometry and circuit quantization, *PRX Quantum* **5**, 020309 (2024).
- [70] S. E. Nigg, H. Paik, B. Vlastakis, G. Kirchmair, S. Shankar, L. Frunzio, M. H. Devoret, R. J. Schoelkopf, and S. M. Girvin, Black-box superconducting circuit quantization, *Phys. Rev. Lett.* **108**, 240502 (2012).
- [71] F. Solgun, D. W. Abraham, and D. P. DiVincenzo, Blackbox quantization of superconducting circuits using exact impedance synthesis, *Phys. Rev. B* **90**, 134504 (2014).
- [72] X. You, J. A. Sauls, and J. Koch, Circuit quantization in the presence of time-dependent external flux, *Phys. Rev. B* **99**, 174512 (2019).
- [73] S. Rasmussen, K. Christensen, S. Pedersen, L. Kristensen, T. Bækgaard, N. Loft, and N. Zinner, Superconducting circuit companion—an introduction with worked examples, *PRX Quantum* **2**, 040204 (2021).
- [74] A. Parra-Rodríguez and I. L. Egusquiza, Geometrical description and Faddeev-Jackiw quantization of electrical networks, *Quantum* **8**, 1466 (2024).
- [75] O. J. Zobel, Theory and design of uniform and composite electric wave-filters, *The Bell System Technical Journal* **2**, 1 (1923).
- [76] [sircuitenum/README.md at main · eliweissler/sircuitenum](#) (2024).
- [77] A. D. Paolo, A. L. Grimsmo, P. Groszkowski, J. Koch, and A. Blais, Control and coherence time enhancement of the $0-\pi$ qubit, *New Journal of Physics* **21**, 043002 (2019).
- [78] A. A. Houck, J. Koch, M. H. Devoret, S. M. Girvin, and R. J. Schoelkopf, Life after charge noise: recent results with transmon qubits, *Quantum Information Processing* **8**, 105 (2009).
- [79] K. V. Price, R. M. Storn, and J. A. Lampinen, Benchmarking Differential Evolution, in *Differential Evolution: A Practical Approach to Global Optimization* (Springer Berlin Heidelberg, Berlin, Heidelberg, 2005) pp. 135–187.
- [80] R. Manenti, E. A. Sete, A. Q. Chen, S. Kulshreshtha, J.-H. Yeh, F. Oruc, A. Bestwick, M. Field, K. Jackson, and S. Poletto, Full control of superconducting qubits with combined on-chip microwave and flux lines, *Applied Physics Letters* **119**, 144001 (2021).
- [81] F. Arute, K. Arya, R. Babbush, D. Bacon, J. C. Bardin, R. Barends, R. Biswas, S. Boixo, F. G. S. L. Brandao, D. A. Buell, B. Burkett, Y. Chen, Z. Chen, B. Chiaro, R. Collins, W. Courtney, A. Dunsworth, E. Farhi, B. Foxen, A. Fowler, C. Gidney, M. Giustina, R. Graff, K. Guerin, S. Habegger, M. P. Harrigan, M. J. Hartmann, A. Ho, M. Hoffmann, T. Huang, T. S. Humble, S. V. Isakov, E. Jeffrey, Z. Jiang, D. Kafri, K. Kechedzhi, J. Kelly, P. V. Klimov, S. Knysh, A. Korotkov, F. Kostritsa, D. Landhuis, M. Lindmark, E. Lucero, D. Lyakh, S. Mandrà, J. R. McClean, M. McEwen, A. Megrant, X. Mi, K. Michielsen, M. Mohseni, J. Mutus, O. Naaman, M. Neeley, C. Neill, M. Y. Niu, E. Ostby, A. Petukhov, J. C. Platt, C. Quintana, E. G. Rieffel, P. Roushan, N. C. Rubin, D. Sank, K. J. Satzinger, V. Smelyanskiy, K. J. Sung, M. D. Trevithick, A. Vainsencher, B. Villalonga, T. White, Z. J. Yao, P. Yeh, A. Zalcman, H. Neven, and J. M. Martinis, Quantum supremacy using a programmable superconducting processor, *Nature* **574**, 505 (2019).
- [82] C. Berke, E. Varvelis, S. Trebst, A. Altland, and D. P. DiVincenzo, Transmon platform for quantum computing challenged by chaotic fluctuations, *Nature Communications* **13**, 2495 (2022).
- [83] L. B. Nguyen, Y.-H. Lin, A. Somoroff, R. Mencia, N. Grabon, and V. E. Manucharyan, High-Coherence Fluxonium Qubit, *Physical Review X* **9**, 041041 (2019).
- [84] H. Zhang, S. Chakram, T. Roy, N. Earnest, Y. Lu, Z. Huang, D. Weiss, J. Koch, and D. I. Schuster, Universal Fast-Flux Control of a Coherent, Low-Frequency Qubit, *Physical Review X* **11**, 011010 (2021).
- [85] F. Bao, H. Deng, D. Ding, R. Gao, X. Gao, C. Huang, X. Jiang, H.-S. Ku, Z. Li, X. Ma, X. Ni, J. Qin, Z. Song, H. Sun, C. Tang, T. Wang, F. Wu, T. Xia, W. Yu, F. Zhang, G. Zhang, X. Zhang, J. Zhou, X. Zhu, Y. Shi, J. Chen, H.-H. Zhao, and C. Deng, Fluxonium: An Alternative Qubit Platform for High-Fidelity Operations, *Physical Review Letters* **129**, 010502 (2022).
- [86] A. Somoroff, P. Truitt, A. Weis, J. Bernhardt, D. Yohannes, J. Walter, K. Kalashnikov, M. Renzullo, R. A. Mencia, M. G. Vavilov, V. E. Manucharyan, I. V. Vernik, and O. A. Mukhanov, Fluxonium qubits in a flip-chip package, *Physical Review Applied* **21**, 024015 (2024).
- [87] A. Somoroff, Q. Ficheux, R. A. Mencia, H. Xiong, R. Kuzmin, and V. E. Manucharyan, Millisecond Co-

- herence in a Superconducting Qubit, *Physical Review Letters* **130**, 267001 (2023).
- [88] I. N. Moskalenko, I. A. Simakov, N. N. Abramov, A. A. Grigorev, D. O. Moskalev, A. A. Pishchimova, N. S. Smirnov, E. V. Zikiy, I. A. Rodionov, and I. S. Besedin, High fidelity two-qubit gates on fluxoniums using a tunable coupler, *npj Quantum Information* **8**, 1 (2022).
- [89] R. A. Mencia, W.-J. Lin, H. Cho, M. G. Vavilov, and V. E. Manucharyan, *Integer Fluxonium Qubit* (2024), arXiv:2403.16780 [quant-ph].
- [90] I. V. Pechenezhskiy, R. A. Mencia, L. B. Nguyen, Y.-H. Lin, and V. E. Manucharyan, The superconducting quasicharge qubit, *Nature* **585**, 368 (2020), publisher: Nature Publishing Group.
- [91] L. Chirolli, M. Carrega, and F. Giazotto, The quartic Blochonium: an anharmonic quasicharge superconducting qubit, *Quantum* **7**, 1193 (2023).
- [92] M. H. Devoret and R. J. Schoelkopf, Superconducting circuits for quantum information: An outlook, *Science* **339**, 1169 (2013).
- [93] E. Hyyppä, S. Kundu, C. F. Chan, A. Gunyhó, J. Hottari, D. Janzso, K. Juliusson, O. Kiuru, J. Kotilahti, A. Landra, W. Liu, F. Marxer, A. Mäkinen, J.-L. Orgiazzi, M. Palma, M. Savitskiy, F. Tosto, J. Tuorila, V. Vadimov, T. Li, C. Ockeloen-Korppi, J. Heinsoo, K. Y. Tan, J. Hassel, and M. Möttönen, Unimon qubit, *Nature Communications* **13**, 6895 (2022).
- [94] D. Kalacheva, G. Fedorov, J. Zotova, S. Kadyrmetov, A. Kirkovskii, A. Dmitriev, and O. Astafiev, *Kinemon: inductively shunted transmon artificial atom* (2023), arXiv:2306.05830 [cond-mat, physics:quant-ph].
- [95] P. Guilmin, R. Gautier, A. Bocquet, and É. Genois, *Dynamiqs: an open-source python library for gpu-accelerated and differentiable simulation of quantum systems* (2024).
- [96] A. Y. Song and X. Croot, private communication (2024).
- [97] A. Di Paolo, T. E. Baker, A. Foley, D. Sénéchal, and A. Blais, Efficient modeling of superconducting quantum circuits with tensor networks, *npj Quantum Information* **7**, 11 (2021).
- [98] N. E. Frattini, U. Vool, S. Shankar, A. Narla, K. M. Sliwa, and M. H. Devoret, 3-wave mixing Josephson dipole element, *Applied Physics Letters* **110**, 222603 (2017).
- [99] Y. Ye, K. Peng, M. Naghiloo, G. Cunningham, and K. P. O'Brien, Engineering purely nonlinear coupling between superconducting qubits using a quarton, *Phys. Rev. Lett.* **127**, 050502 (2021).
- [100] J. E. Mooij and Y. V. Nazarov, Superconducting nanowires as quantum phase-slip junctions, *Nature Physics* **2**, 169 (2006).
- [101] F. Motzoi, J. M. Gambetta, P. Rebentrost, and F. K. Wilhelm, Simple pulses for elimination of leakage in weakly nonlinear qubits, *Phys. Rev. Lett.* **103**, 110501 (2009).
- [102] J. M. Gambetta, F. Motzoi, S. T. Merkel, and F. K. Wilhelm, Analytic control methods for high-fidelity unitary operations in a weakly nonlinear oscillator, *Phys. Rev. A* **83**, 012308 (2011).
- [103] D. D. Stancil and G. T. Byrd, *Principles of superconducting quantum computers* (John Wiley & Sons, 2022).